Journal of Colloid and Interface Science 688 (2025) 22–31

Contents lists available at ScienceDirect

Journal of Colloid And Interface Science

journal homepage: www.elsevier.com/locate/jcis

PtO nanoclusters on ultra-thin 2D Mo_2C enhance hydrated cation interaction for superior alkaline hydrogen evolution reaction

Lei Xiang [a,1], Difei Leng [a,1], Xuming Zhang [a,*], Han Li [a], Handu Wang [a], Chaoran Pi [b,*], Shuangjie Wu [d], Li Huang [d], Yun Li [d], Kaifu Huo [c], Paul K. Chu [e]

[a] State Key Laboratory of Advanced Refractories, School of Metallurgy and Energy, Institute of Advanced Materials and Nanotechnology, Wuhan University of Science and Technology, Wuhan 430081, China
[b] School of Optoelectronic Materials and Technology, Jianghan University, Wuhan 430056, China
[c] Wuhan National Laboratory for Optoelectronics (WNLO), School of Optical and Electronic Information, Huazhong University of Science and Technology, Wuhan 430074, China
[d] Guizhou Wujiang Hydropower Development Co, LTD, Guiyang 550002, China
[e] Department of Physics, Department of Materials Science and Engineering, Department of Biomedical Engineering, City University of Hong Kong, Tat Chee Avenue, Kowloon, Hong Kong, China

GRAPHICAL ABSTRACT

PtO nanoclusters modified 2D Mo_2C is designed and fabricated by a molten salt method combined with a simple liquid-phase deposition technique, which demonstrates significant interfacial charge reconstruction and strong electrostatic interaction with hydrated cation, leading to remarkable alkaline HER performance by a kinetically fast Volmer-Tafel pathway.

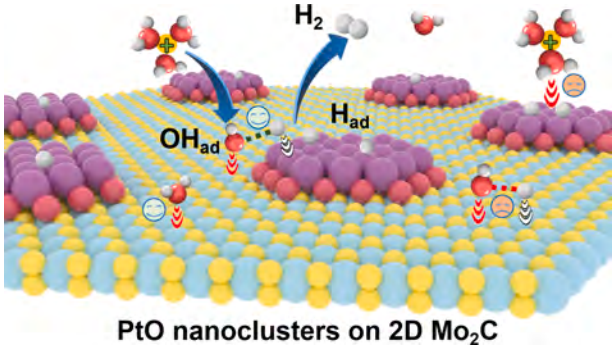

ARTICLE INFO

Keywords:
Alkaline hydrogen evolution reaction
Two-dimensional molybdenum carbide
PtO nanoclusters
Interfacial water
In situ Raman scattering

ABSTRACT

Platinum oxide (PtO) is regarded as an effective catalyst beyond platinum metal for the hydrogen evolution reaction (HER). However, slow kinetics and structural instability limit its wide application as alkaline electrocatalyst. Herein, PtO nanoclusters decorated ultrathin two-dimensional (2D) Mo_2C with a Pt concentration of 0.98 wt% (Mo_2C-PtO) is designed and prepared to overcome these hurdles. The Mo_2C-PtO catalyst shows significant interfacial charge reconstruction and strong electrostatic interaction with hydrated ions and exhibits remarkable HER performance with an ultra-low overpotential of 5, 64 and 329 mV at 10, 100 and 1000 mA cm^{-2}

* Corresponding authors.
E-mail addresses: xumingzhang@wust.edu.cn (X. Zhang), chaoran_pi@foxmail.com (C. Pi).
[1] These authors contributed equally to this work.

https://doi.org/10.1016/j.jcis.2025.02.103
Received 20 December 2024; Received in revised form 13 February 2025; Accepted 15 February 2025
Available online 18 February 2025

and a small Tafel slope of 25 mV dec^{-1} in alkaline solution, as well as the long-term durability of hydrogen production at 500 mA cm^{-2}. *In situ* Raman scattering and theoretical calculation reveal the fast migration and dissociation of cationic hydration water at interface, which accelerates Volmer reaction. The key intermediates of OH* and H* transfer rapidly from the interface to Mo_2C and PtO, respectively, which increases the availability of interfacial sites and facilitates the fast Volmer-Tafel mechanism. This study highlights the potential of carbide-supported PtO nanoclusters as highly efficient catalysts for alkaline hydrogen production and offers insights into the interfacial water evolution mechanism.

1. Introduction

Hydrogen is a desirable alternative to fossil fuels due to its high energy density and zero carbon emissions, and water electrolysis powered by renewable energy has gained significant attention as a sustainable and cost-effective method to produce green hydrogen [1]. Recently, the alkaline hydrogen evolution reaction (HER) has attracted interest because of the high tolerance of most catalysts and better safety for electrolytic devices compared to acidic HER [2,3]. However, the additional energy barrier associated with water dissociation in an alkaline medium results in high overpotentials and slow kinetics [4–6].

Platinum (Pt)-based catalysts are well-known for their superior hydrogen binding energy in acidic condition [1,7–9]. In order to reduce the cost, efforts have been made to reduce the Pt concentration by using Pt clusters, alloys, and single-atom catalysts [10–13]. Recent research has shown that PtO_x catalysts outperform metallic Pt^0 due to the longer Pt-O bond, which facilitates proton-electron coupling and accelerates H_2 release [14–17]. For instance, Yang et al. have synthesized single-layer 1 *T*-phase metastable platinum oxide (1 T-PtO_2) by a molten-alkali mechanochemical method, achieving impressive HER activity with a low overpotential of 12 mV at 10 mA cm^{-2} in the acid medium [18]. However, the PtO catalyst still encounters challenges in reducing the activation barrier for water dissociation and improving OH_{ad} transfer under alkaline conditions [19]. Recently, the significance of hydrated cations in water electrolysis has gained much attention [20–22]. For example, Li et al. found that the large work function of high-valence RuO_2 on Ru metal surfaces enhances its interaction with hydrated cations, improving interfacial water adsorption and dissociation while modifying the adsorption energies of active H and OH species [6]. Therefore, in order to develop effective catalysts for alkaline hydrogen production, it is crucial to comprehend the dynamics of interfacial water and key intermediates on the catalyst surface.

To enhance interfacial water interactions, catalysts are often supported by substrates that can stabilize and improve their electrocatalytic performance, and broaden their application range [16]. Various substrates such as carbonaceous materials, oxides, carbides, nitrides, sulfides, and hydroxides have been explored for loading metal-based catalysts with strong metal-support interaction for alkaline HER [16,23–29]. Notably, transition metal carbides (TMCs) are distinguished by their Pt-like electronic structure, excellent corrosion resistance, and metallic conductivity [20,30–33]. Some metal-carbide composites have been developed for advanced MOR, HER and ORR reactions [23,34,35]. The interactions between the metal catalyst and substrate can not only provide abundant high active sites [36], but also modulate their electronic structure, enhancing the reaction efficiency [37–39]. Consequently, it is reasonable to anticipate that Mo_2C loaded with PtO nanoclusters could exhibit excellent HER performance in alkaline solutions. However, challenges remain in optimizing the size, distribution, and loading mass of PtO clusters on Mo_2C through scalable and reproducible synthesis methods due to the significant aggregation of nanomaterials and the catalyst-support interaction with interfacial water in modulating the HER kinetics are still remain inadequately elucidated and necessitate a more comprehensive exploration.

Herein, PtO clusters supported by ultrathin 2D Mo_2C nanosheets (Mo_2C-PtO) are prepared by a molten salt method combined with a simple liquid-phase deposition technique. The PtO clusters with ~ 2 nm in size are uniformly distributed on ~ 4 nm thick 2D Mo_2C nanosheets. The different work functions promote electron transfer from Mo_2C to PtO, leading to a lot of electrons to accumulate at the interface. *In situ* Raman scattering and density-functional theory (DFT) simulations reveal that the rapid migration of hydrated cations towards the interface and high adsorption energy of OH* species on Mo_2C are pivotal for water adsorption and dissociation at this junction. Furthermore, the interaction between Mo_2C and PtO optimizes the adsorption affinity for H* at PtO catalyst, thereby expediting HER activity by kinetically fast Volmer-Tafel pathway. The optimized Mo_2C-PtO catalyst with 0.98 wt% Pt demonstrates exceptional electrocatalytic performance, highlighted by an ultralow overpotential of 5 mV to achieve a current density of 10 mA cm^{-2}, a minimal Tafel slope of 24 mV dec^{-1} and remarkable stability at different current densities for over 300 h in alkaline solution. This study offers valuable insights into catalyst-substrate interactions during alkaline HER and guidance for designing Pt-based catalysts for alkaline electrochemical reactions.

2. Experiment details

2.1. Materials

Potassium hydroxide (KOH AR, ≥85 %), potassium monobasic phosphate (KH_2PO_4 AR, ≥99.5 %), dipotassium phosphate (K_2HPO_4 AR, ≥99.5 %), anhydrous sodium carbonate (Na_2CO_3 AR, ≥99.5 %), and absolute ethanol (CH_3CH_2OH AR, 99.7 %) isopropanol ($(CH_3)_2CHOH$ AR, ≥99.7 %) were purchased from Sinopharm Chemical Reagent Co., Ltd. Molybdenum disulfide (MoS_2, AR, ≥99.5 %), urea ($CO(NH_2)_2$, AR, ≥99.5 %), nafion117 solution (5 % concentration), and chloroplatinic acid hexahydrate ($H_2PtCl_6{\cdot}6H_2O$ ACS, Pt 37.5 %) were sourced from Shanghai Aladdin Biochemical Technology Co., Ltd. The platinum on carbon catalyst (Pt/C 20 wt%) was purchased from Johnson Matthey Co., Ltd. All the reagents and materials were used as received without purification.

2.2. Synthesis of 2D Mo_2C nanosheets

Typically, 640 mg of molybdenum disulfide (MoS_2) and 1,272 mg of sodium carbonate (Na_2CO_3) were combined and ground in a mortar. 5 mL of deionized water was mixed with Na_2CO_3 to create a slurry, which was then ground for 1 h. The slurry was oven-dried, then 3 g of urea was added and ground until no large particles remained. The resulting powder was placed in a tubular furnace and heated to 800 °C for 6 h in a 7 vol% H_2/Ar atmosphere, forming a black lumpy material. This material was then stirred with 1 M sulfuric acid (H_2SO_4) for 2 h, filtered, and air-dried to produce black 2D Mo_2C powder.

2.3. Synthesis of Mo_2C-PtO

To synthesize the PtO nanoclusters modified 2D Mo_2C catalyst, $H_2PtCl_6{\cdot}6H_2O$ (0.5 mg, 1 mg, and 2 mg) was added to 25 mL of deionized water containing 25 mg of 2D Mo_2C powder. The composites with initial Pt concentrations of 0.8 wt%, 1.6 wt%, and 3.2 wt% were labeled Mo_2C-PtO-1, Mo_2C-PtO-2, and Mo_2C-PtO-3, respectively. After sonication for 1 h, the suspension was transferred to an 80 mL Polytetrafluoroethylene (PTFE) flask, sealed, and heated in a water bath at 90 °C

with continuous agitation for 1 h. Then, the product was retrieved by filtration and lyophilization.

2.4. Materials characterization

The crystalline structure of the samples was analyzed by X-ray diffraction (XRD) (Rigaku SmartLab) with Cu K_α radiation ($\lambda = 1.5405$ Å). The morphology of the catalysts was examined by scanning electron microscopy (SEM) (ThermoFisher Apreo S HiVac) and high-resolution transmission electron microscopy (HR-TEM) (JEM-2100 UHR STEM). X-ray photoelectron spectroscopy (XPS) was performed to determine the chemical states (Thermo Scientific Escalab 250Xi), and Raman scattering was conducted on the RamLab HR 800 Raman Microscope.

2.5. Electrochemical measurements

Electrochemical evaluations were conducted on the VSP-300 electrochemical workstation (Biologic Science Instruments, France) with a three-electrode setup in 1.0 M KOH, 0.5 M H_2SO_4, or 1.0 M PBS. The synthesized electrocatalyst serves as the working electrode, which was prepared by dispersing 5 mg of the catalyst in a 1 mL water/ethanol solution (v/v = 1:1) with 20 μL of Nafion to form a slurry. The slurry was pasted onto a piece of Ni foam (1×1 cm^2) in several times and dried in a vacuum oven. The Hg/HgO electrode and graphite rod were the reference and counter electrodes, respectively. For comparison, a Ni foam loaded with an amount equivalent to 20 wt% commercial Pt/C was prepared. The polarization curves were referenced to the reversible hydrogen electrode (RHE) by the equation: E (vs. RHE) = E (vs. Hg/HgO) + 0.0592 × pH + 0.098 V, with 80 % *iR* compensation. Linear sweep voltammetry (LSV) was performed from −0.9 V to −1.5 V vs. Hg/HgO at 5 mV s^{-1}. The Tafel plots were derived in the linear regions by the Tafel equation ($\eta = a + b \log j$), where η is the overpotential, b represents the Tafel slope, and j is the current density. Electrochemical impedance spectroscopy (EIS) was carried out in the frequency range between 10^{-2} and 10^5 Hz at a 10 mV overpotential and with 5 mV amplitude perturbation. The double-layer capacitance (C_{dl}) was determined from the cyclic voltammetry (CV) curves in the non-Faradaic region between −0.85 to −0.95 V (vs. Hg/HgO) at various scanning rates (10, 12, 14, 16, and 18 mV s^{-1}). The ECSA was calculated by the following equation: ECSA = C_{dl}/40 μF cm^{-2}, and the electrochemical stability was assessed by chronoamperometry testing with different initial current densities for different time periods.

2.6. In situ Raman scattering

Raman scattering was performed on the LabRAM HR 800 system with a 532 nm Nd:YAG laser. The Raman frequency calibration was done using a silicon wafer as a standard. In the electrochemical cell, the carbon rod was the counter electrode and the Hg/HgO electrode served as the reference. Potential control was managed by an electrochemical workstation (CHI 760 D, Chenhua, China). The spectral data were collected using 60 s exposure and were accumulated in duplicate at different potentials.

2.7. Density functional theory calculations

Density functional theory (DFT) calculations were performed using CP2K with a cutoff energy of 400 Ry [40], based on the PtO (002), Mo_2C (101), and Pt_4O_4 cluster/Mo_2C (101) heterostructure models. The pbe-sol functional, based on the generalized gradient approximation, was used for the exchange–correlation potential during geometry optimization, employing the DZVP-MOLPOT-SR-GTH basis set and pseudopotential. Convergence criteria were set at 10^{-12} for EPS_DEFAULT and 10^{-6} for EPS_SCF, with a k-point grid of $5 \times 4 \times 4$ for sampling the first Brillouin zone of Mo_2C. A Mo_2C supercell measuring $2 \times 4 \times 2$ was constructed post-optimization, featuring a 15 Å vacuum layer in the (101) direction, while all atoms except for surface ones were constrained to achieve full relaxation. This setup enabled the construction of the Pt_4O_4 cluster/Mo_2C (101) model, which utilized a k-point grid of $2 \times 2 \times 1$, maintaining convergence thresholds of 10^{-12} for EPS_DEFAULT and 10^{-6} for EPS_SCF.

For energy calculations, the GTH-PBE functional under the generalized gradient approximation was employed, alongside the TZV2P-MOLOPT-SR-GTH basis set and pseudopotential, with convergence limits set to 10^{-14} for EPS_DEFAULT and 10^{-7} for EPS_SCF. Relevant thermodynamic quantities were calculated using Shermo [41], with the Gibbs free energy change (ΔG) for each elementary step derived from the computational hydrogen electrode model: $\Delta G = \Delta E + \Delta ZPE - T\Delta S$, where ΔE is obtained from DFT, ΔZPE is the change in zero-point energies, T is the temperature (298.15 K), and ΔS is the change in entropy of products and reactants.

In the transition state analysis for H_2O decomposition into H and OH on the catalyst surface, the CI-NEB method was utilized to interpolate 10 points between initial and final states to identify the transition state. The exchange–correlation potential was approximated using the pbe-sol functional with the DZVP-MOLPOT-SR-GTH basis set and pseudopotential, maintaining convergence limits of 10^{-12} for EPS_DEFAULT and 10^{-6} for EPS_SCF.

2.8. Assembly and electrocatalytic properties of anionic membrane electrolyzer

The electrolyzer consisted of an anode (1 cm^2, 5 mg Mo_2C-PtO-2), a cathode (1 cm^2, NiFe LDH on Ni foam), and anionic membrane (Sustainion X37-50 Grade 60). The 50 μm thick, 6.25 cm^2 anionic membrane was pre-soaked in 1 M KOH for 24 h. The anode was prepared by drop-casting 5 mg of Mo_2C-PtO-2 onto 1 cm^2 Ni foam, with 5 mg of 20 % Pt/C on 1 cm^2 Ni foam for comparison. The NiFe-LDH nanosheets were grown directly on the Ni foam to form the cathode. Specifically, a 1×1 cm^2 Ni foam was immersed in 0.4 M $Fe(NO_3)_3$ solution for several seconds, then air-dried for 10 min and dipped into 2 M NaOH for 1 min, which was further extracted rapidly, and air-dried to form the brown NiFe-LDH coating. After assembly, the water electrolysis properties of the AEM electrolyzer were determined in 1 M KOH at ambient temperature. After assembly, the water splitting performance was tested in 1 M KOH at ambient temperature. The durability was assessed at a current density of 500 mA cm^{-2} (1.84 V) for 100 h at room temperature.

3. Results and discussion

The synthesis of PtO-nanoclusters-decorated 2D Mo_2C nanosheets is illustrated in Fig. 1a. Firstly, 2D Mo_2C is produced by the molten salt method from commercial MoS_2 precursors [42]. Bulk MoS_2 with a stacked layered structure and an average size of 50 μm (Fig. S1a) reacts with urea at 800 °C under Ar/H_2 in the presence of Na_2CO_3. Subsequent washing processes yield hexagonal β-Mo_2C product (PDF No. 65–8766) confirmed by XRD (Fig. S1b). No residual MoS_2 is detected, indicating complete conversion from MoS_2 to Mo_2C [20]. The transmission electron microscopy (TEM) image reveals the high crystallinity of the 2D Mo_2C structure (Fig. S2). After the hydrothermal treatment in the presence of $H_2PtCl_6{\cdot}6H_2O$ at 90 °C for 2 h, Fig. 1b shows a smooth surface. Atomic force microscopy (AFM) discloses a 2D structure with a thickness of 3.5 ± 0.5 nm and surface roughness of ~ 0.2 nm (Fig. 1c). XRD shows no peaks related to Pt metal or PtO from the product with a low $H_2PtCl_6{\cdot}6H_2O$ content, except the β-Mo_2C peaks at 34.5°, 38.0°, and 39.6° (Fig. 1d and Fig. S3). This may be attributed to the small size and small PtO content. When the concentration of $H_2PtCl_6{\cdot}6H_2O$ is raised to 2 mg (Pt feeding ratio of ~ 3 wt%, sample labeled as Mo_2C-PtO-3), a small diffraction peak emerges at 33.5° corresponding to the PtO (002) plane (PDF No. 85–0714) [43]. High-resolution transmission electron microscopy (HR-TEM) (Fig. 1e and f) shows lattice spacings of 0.228 for Mo_2C (1 0 1) and 0.266 nm for PtO (0 0 2), consistent with XRD. High-

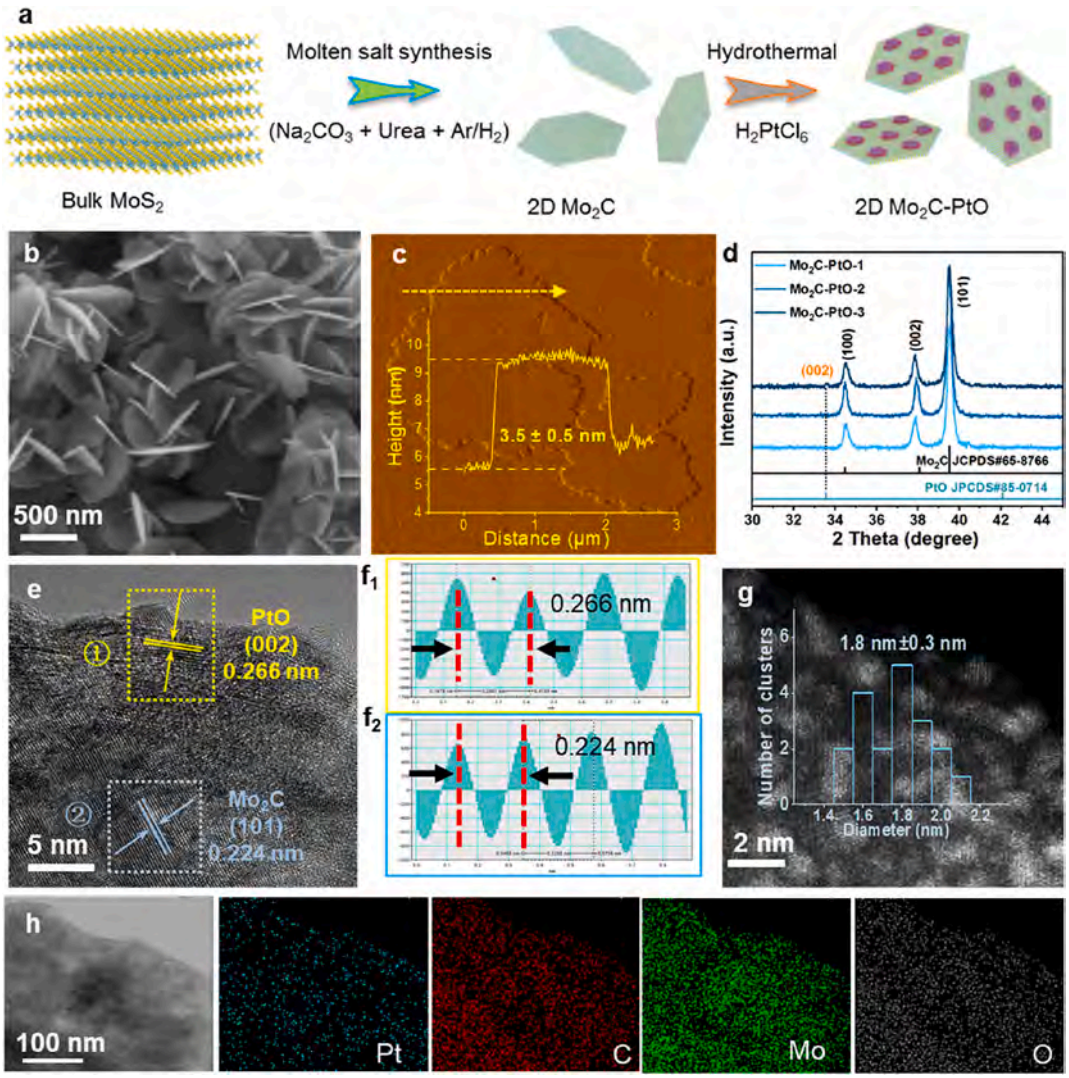

Fig. 1. (a) Schematic illustration of the preparation of PtO nanoclusters on 2D Mo_2C crystals by the molten salt method and subsequent liquid-phase deposition; (b, c) SEM and AFM images of Mo_2C-PtO-2; (d) XRD spectra of Mo_2C-PtO-1, Mo_2C-PtO-2, and Mo_2C-PtO-3; (e, f) TEM image and interplanar spacing profiles of Mo_2C-PtO-2; (g) HAADF-STEM image and (h) EDS elemental maps of Mo_2C-PtO-2.

angle annular dark-field scanning transmission electron microscopy (HAADF-STEM) is performed to examine the arrangement of Pt species (Fig. 1g), and ~ 2 nm Pt cluster species are observed from the Mo_2C surface, confirming successful immobilization of PtO clusters on Mo_2C. Energy-dispersive X-ray spectroscopy (EDS) (Fig. 1h) confirms the uniform distributions of Mo, Pt, C, and O. All the results suggest an ultrathin PtO nanoclusters decorated on 2D Mo_2C. Inductively-coupled plasma mass spectrometry (ICP-MS) shows that the Pt concentrations in Mo_2C-PtO-1, Mo_2C-PtO-2, and Mo_2C-PtO-3 are 0.42 wt%, 0.98 wt%, and 2.63 wt%, respectively (Fig. S4). The corresponding utilization rates of Pt are 52.5 %, 61.3 %, and 82.2 %. In Mo_2C-PtO-1, ~1.5 nm Pt clusters with poor crystallinity are distributed uniformly on Mo_2C (Fig. S5), whereas Mo_2C-PtO-3 shows enhanced crystallinity and larger Pt clusters of 5.1 ± 3 nm (Fig. S6).

The surface chemistry and electronic properties of Mo_2C-PtO are analyzed by X-ray photoelectron spectroscopy (XPS). The survey spectrum in Fig. S7 shows the presence of Mo, O, Pt, and C but no Cl 2*p* peak, consistent with EDS. The Pt 4*f* spectrum of the Pt/C catalyst reveals dominant metallic states of Pt^0 at 71.2 eV and 74.4 eV, but no metallic Pt signals are detected from Mo_2C-PtO (Fig. S8). Fig. 2a depicts the high-resolution Pt 4*f* spectrum of Mo_2C-PtO-2, which can be deconvoluted into two pairs of characteristic peaks representing dominant Pt^{2+} (72.4 and 75.6 eV) and minor Pt^{4+} (73.5 and 76.7 eV) with an area ratio of 4 to 1 [44]. The high-valence Pt^{4+} likely results from oxidation upon air exposure. These observations confirm the formation of PtO clusters without Pt^0 species on the 2D Mo_2C surface. Fig. 2b presents the Mo 3*d* spectra of both Mo_2C and PtO-modified Mo_2C. The Mo 3*d* spectrum of pure Mo_2C (Mo $3d_{3/2}$ and Mo $3d_{5/2}$) can be deconvoluted into doublet peaks at 228.2 and 231.3 eV corresponding to Mo-C bonds, while the other peaks are attributed to Mo-O bonds indicated by Mo^{4+} (228.9 and 232.0 eV) and Mo^{6+} (232.6 and 235.7 eV) [45]. Upon coupling with PtO clusters, the Mo-C and Mo-O bonds exhibit positive shifts of 0.2 eV and 0.3 eV, respectively, suggesting electron transfer from Mo_2C to PtO. The strong interaction enhances the bonding strength between the Mo_2C substrate and PtO clusters. The XPS C 1 *s* spectra of Mo_2C and Mo_2C-PtO show four peaks at 283.3, 284.8, 286.3, and 288.8 eV, corresponding to C-Mo, C—C, C—O, and C═O respectively (Fig. S8). The O 1 *s* spectra of Mo_2C reveal peaks of Mo-O (530.0 eV) and adsorbed O_{ads} (531.5 eV). As for Mo_2C-PtO, an additional Pt-O peak appears at 529.4 eV and increases with the PtO mass loading.

To understand the electron transfer mechanism, the work functions (Φ) of Mo_2C, PtO, and Mo_2C-PtO are calculated. The energy required for electrons to escape from the Fermi level with a potential well of depth X is defined as Φ. A smaller Φ translates into easier electron escape. The

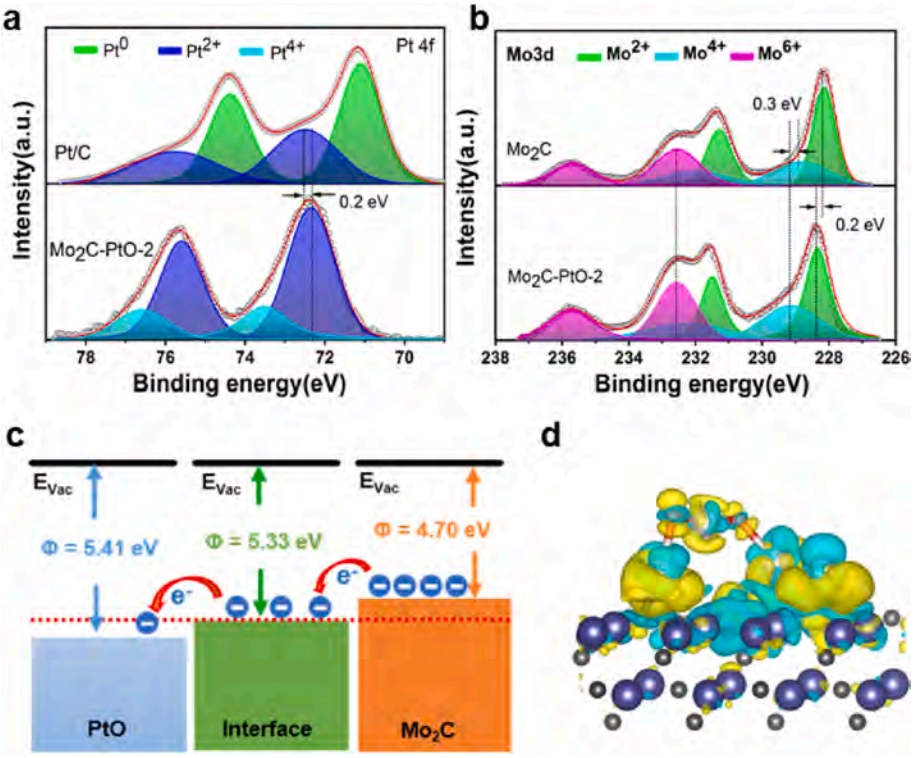

Fig. 2. (a, b) XPS Pt 4*f* and Mo 3*d* spectra of Mo_2C-PtO-2; (c) Work functions of PtO, Mo_2C-PtO, and Mo_2C; (d) Lateral views showing the charge density difference in Mo_2C-PtO, where the yellow and cyan regions represent electron accumulation and depletion, respectively. (For interpretation of the references to colour in this figure legend, the reader is referred to the web version of this article.)

calculations indicate that the work function of Mo_2C-PtO ($\Phi = 5.33$ eV) lies between PtO ($\Phi = 5.41$ eV) and Mo_2C ($\Phi = 4.70$ eV) (Fig. S9). An inherent electric field forms at the interface when Mo_2C and PtO are coupled to drive charge transfer from Mo_2C to PtO until equilibrium. The work function of Mo_2C-PtO is closer to that of PtO but significantly higher than that of Mo_2C, suggesting a large accumulation of electrons at the Mo_2C-PtO interface (Fig. 2c). The charge difference analysis imparts information about the interfacial characteristics and electron distributions of Mo_2C-PtO. As shown in Fig. 2d, more electrons aggregate at the interface and towards the PtO, which make the interface has a stronger electrostatic interaction. The electron reconstruction is consistent with the XPS results and work functions, highlighting the charge balance mechanism at Mo_2C-PtO interface.

The electrocatalytic properties of the 2D Mo_2C-PtO catalyst for the hydrogen evolution reaction (HER) are assessed using a three-electrode system in 1.0 M KOH solution and compared with those of 20 wt% Pt/C and 2D Mo_2C catalysts. The polarization curves are automatically iR-corrected. Fig. 3a indicates that Mo_2C-PtO-2 has the best HER characteristics, requiring overpotentials of 5, 64, and 329 mV to reach current densities of 10, 100, and 1000 mA cm^{-2}, respectively, which outperform those of Mo_2C-PtO-1, Mo_2C-PtO-3, 2D Mo_2C, and commercial 20 wt% Pt/C (Fig. 3b and Fig. S10). The optimal Mo_2C-PtO-2 catalyst exhibits a Tafel slope of 24 mV dec^{-1}, which is smaller than those of Mo_2C-PtO-1 (52 mV dec^{-1}), Mo_2C-PtO-3 (38 mV dec^{-1}), Mo_2C (130 mV dec^{-1}), and Pt/C (29 mV dec^{-1}), indicating that the Volmer-Tafel mechanism dominates under alkaline conditions and the Tafel step is the rate-limiting process (Fig. 3c) [46]. The large Tafel slope of bare Mo_2C (>120 mV dec^{-1}) suggests that the Volmer reaction is the rate-determining step. After coupling with PtO clusters, the double-layer capacitances (C_{dl}) of Mo_2C-PtO-1, Mo_2C-PtO-2, and Mo_2C-PtO-3 are approximately 2.1, 2.5, and 1.9 times that of the bare 2D Mo_2C due to more catalytically active sites from PtO (Fig. S11). The Mo_2C-PtO-2 catalyst also shows a small charge transfer resistance (R_{ct}) of 0.45 Ω compared with Mo_2C-PtO-1 (1.32 Ω), Mo_2C-PtO-3 (5.21 Ω), Mo_2C (30.50 Ω), and Pt/C (7.23 Ω), indicating superior charge transfer efficiency (Fig. 3e).

The mass activity is a crucial parameter to evaluate the catalytic activity and utilization rate of Pt-group metal (PGM)-based catalysts. As for the optimal Mo_2C-PtO-2 catalyst, the mass activity normalized to the loaded Pt amount is significantly higher than those of other catalysts after subtracting the catalytic contribution of the Mo_2C substrate (Fig. 3d). They are 3.5, 8.8, and 14.8 A mg^{-1} at overpotentials of 100, 200, and 300 mV respectively, which are approximately 30 times that of 20 wt% Pt/C (0.1, 0.28, 0.5 A mg^{-1}) (Fig. S12). The results demonstrate that Mo_2C-PtO-2 containing 0.98 wt% Pt has better alkaline HER activity and cost-effectiveness than commercial 20 wt% Pt/C on account of the large exposure of Pt active sites. The stability of the Mo_2C-PtO-2 catalyst is evaluated, and Fig. 3f shows the chronoamperometry testing under alkaline conditions. Remarkably, Mo_2C-PtO-2 maintains exceptional durability with negligible degradation in the HER activity after 300 h when the initial current densities are changed from 50 to 200 mA cm^{-2}. The morphology and crystal structure of Mo_2C-PtO-2 remain unchanged after the stability test (Fig. S13). The main chemical form of Pt is Pt^{2+}, while Mo 3d is primarily associated to Mo_2C, with a minor presence of an oxide state, indicating notable chemical stability (Fig. S14).

The HER activity is also evaluated in neutral (1 M PBS) and acidic (0.5 M H_2SO_4) media. Mo_2C-PtO shows 2–3 times larger C_{dl} than bare 2D Mo_2C under both conditions, similar to the results in alkaline media (Figs. S15 and S16). The electrocatalytic properties of Mo_2C-PtO are slightly inferior to those of commercial 20 wt% Pt/C in neutral and acidic solutions, but the normalized mass activity of Pt in Mo_2C-PtO-2 is 25 and 20 times larger than that of commercial 20 wt% Pt/C under acidic and neutral conditions at an overpotential of 100 mV, respectively (Figs. S17 and S18). The ECSA-normalized LSV curves in all pH range further illustrate the exceptional intrinsic electrocatalytic capability of Mo_2C-PtO-2 compared to the bare 2D Mo_2C, Mo_2C-PtO-1 and Mo_2C-PtO-3 (Fig. S19). The optimal Mo_2C-PtO-2 catalyst also exhibits high stability

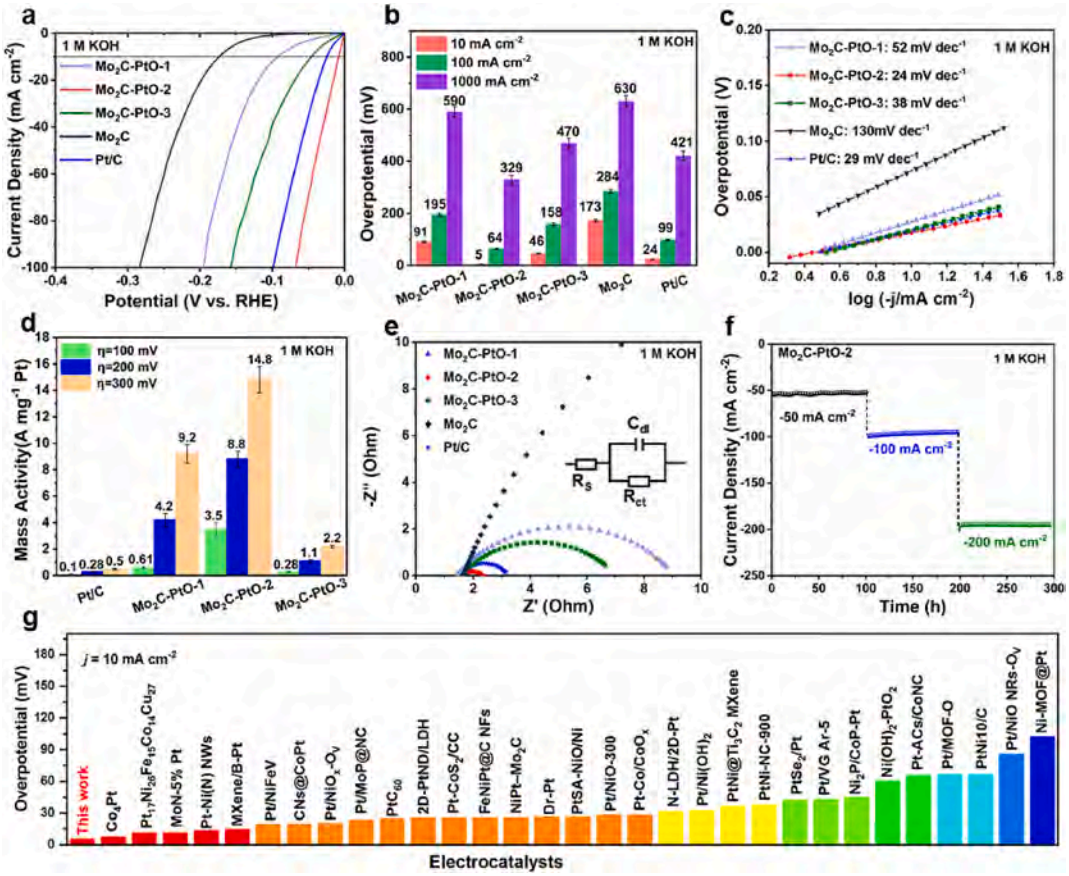

Fig. 3. (a) Polarization curves of Mo_2C-PtO-1, Mo_2C-PtO-2, Mo_2C-PtO-3, 2D Mo_2C, and 20 % Pt/C in 1 M KOH; (b) Overpotentials at different current densities after different measurement (n = 3); (c) Tafel slopes; (d) Mass activities of Pt at 100 mV, 200 mV, and 300 mV after different measurement (n = 3); (e) Nyquist plots; (f) Chronoamperometry testing of Mo_2C-PtO-2 at initial current densities of 50, 100, and 200 mA cm^{-2} in 1 M KOH for 100 h; (g) Comparison of the overpotentials between the optimal Mo_2C-PtO catalyst and recently reported Pt-based electrocatalysts at 10 mA cm^{-2}.

in acidic and neutral environments for 300 h (Fig. S20). In particular, the electrocatalytic properties of optimal Mo_2C-PtO in the alkaline medium are better than most reported PGM-based catalysts (Fig. 3g and Table S1). These results indicate that the effective binding of PtO clusters on 2D Mo_2C enhances the hydrogen evolution activity under alkaline conditions.

Electrocatalytic evaluations reveal that water dissociates rapidly at the Mo_2C-PtO interface to produce active hydrogen species and accelerate alkaline hydrogen evolution. It has been shown that structural changes in interfacial water and migration of key intermediates at the solid–liquid interface impact the electrocatalytic efficiency in alkaline environments [6,10,47]. Raman scattering can be used to monitor the structural changes in surface water molecules and dynamic alterations in surface chemical bonds to provide molecular-level information about catalyst-species interactions [48]. Fig. 4 presents the *in situ* Raman spectra of interfacial water and adsorbed hydrogen on Mo_2C-PtO-2 catalyst in 0.1 M NaOH in the potential range between 0.1 V and −0.4 V (vs. RHE). For comparison, the bare 2D Mo_2C and Pt/C catalysts are also analyzed. Sodium ions (Na^+) with a smaller ionic radius enhance the stability of surrounding hydroxyl groups and water molecules (OH^-–$(H_2O)_x$–Na^+), allowing direct spectroscopic observation of interfacial water dynamics during HER [22]. The Raman peaks in the 2030–2100 cm^{-1} range correspond to the $\nu_{Pt\text{-}H}$ mode of hydrogen atoms coordinated to platinum atoms on the surface [49]. An increase in the $\nu_{Pt\text{-}H}$ bond strength with rising overpotentials suggests that the adsorbed hydrogen intermediates at Pt sites are crucial for HER [34]. The $\nu_{Pt\text{-}H}$ vibration of Mo_2C-PtO-2 is detected at an overpotential of −0.1 V, which is more sensitive than that on Pt/C (Fig. 4a). As the overpotential increases, the normalized intensity of the $\nu_{Pt\text{-}H}$ vibration of Mo_2C-PtO-2 exceeds that of the Pt/C catalyst, indicating superior catalytic performance (Fig. 4b). The band at 1,600–1,650 cm^{-1} corresponds to the H—O—H bending mode ($\delta_{H—O—H}$) of interfacial water [48]. As the overpotential rises, the $\delta_{H—O—H}$ intensity of Mo_2C and Mo_2C-PtO-2 remains similar, but it surpasses that of Pt/C, highlighting the strong interaction between water molecules and Mo_2C as well as Mo_2C-PtO-2. Water contact angle measurements on Pt/C, Mo_2C, and Mo_2C-PtO-2 confirm the water affinity of Mo_2C and Mo_2C-PtO-2, further demonstrating the strong water interaction (Fig. S21).

The broad band between 3,000 and 3,800 cm^{-1} is ascribed to the O—H stretching vibration of interfacial water ($\nu_{O\text{-}H}$), which is highly sensitive to the local chemical environment [50]. The modulation of the adsorbate's vibrational frequency in response to electrode potential variations arises from the vibrational Stark effect, where a steeper Stark tuning rate indicates a higher sensitivity to the local electric field on the electrode surface [6]. The $\nu_{O\text{-}H}$ bond can be decomposed into three Gaussian peaks representing three distinct O—H stretching vibrations. The lower wavenumber component (Fig. 4c, blue area) and the middle component (Fig. 4c, orange area) correspond to 4-coordinated and 2-coordinated hydrogen-bonded water, respectively, while the higher wavenumber component (Fig. 4c, green area) is associated with weakly hydrated water (Na^+–H_2O) [51]. The high intensities of the three peaks suggest that the Raman signals predominantly originate from the water layers of inner Helmholtz layer on the catalyst surface. Notably, the peak area of Na^+–H_2O increases significantly on Mo_2C-PtO-2 at higher overpotentials, indicating a reorientation of the $Na^+{\cdot}H_2O$ structure for more favorable conditions for water adsorption and dissociation. Furthermore, the vibrational frequency of $Na^+{\cdot}H_2O$ on Mo_2C-PtO-2 is lower than that of Pt/C at a more negative potential, suggesting a

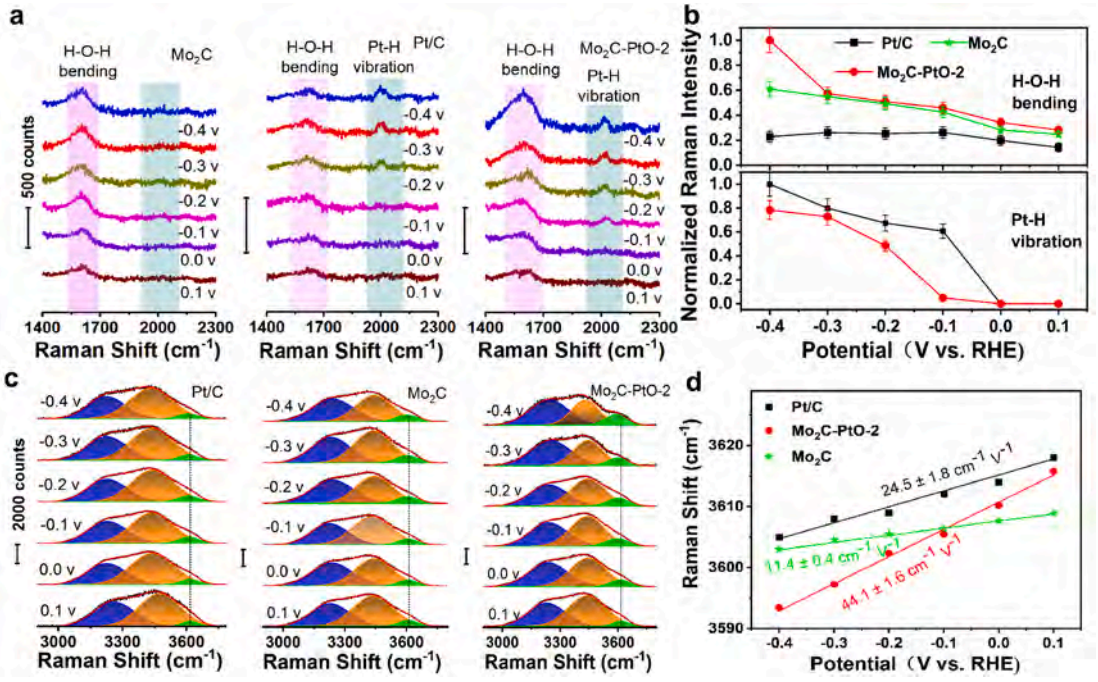

Fig. 4. (a) *In situ* Raman scattering spectra of the alkaline HER process for different overpotentials of 2D Mo_2C, Mo_2C-PtO-2, and commercial Pt/C; (b) Normalized Raman intensities after different measurement (n = 3); (c) *In situ* Raman spectra of interfacial water on 2D Mo_2C, Mo_2C-PtO-2, and commercial Pt/C in 0.1 M NaOH (pH = 13), with the Gaussian fits illustrating the three O—H stretching modes in blue (4-coordinated hydrogen-bonded water), orange (2-coordinated hydrogen-bonded water) and green ($Na^+ \cdot H_2O$); (d) Frequency plot of changes in the ν_{O-H} in Raman spectra of interfacial water at 2D Mo_2C, Mo_2C-PtO-2, and commercial Pt/C surfaces. (For interpretation of the references to colour in this figure legend, the reader is referred to the web version of this article.)

stronger interaction of $Na^+ \cdot H_2O$ on Mo_2C-PtO for rapid interfacial water migration. The Stark tuning rate of $Na^+ \cdot H_2O$ on Pt/C is calculated to be 24.5 ± 1.8 $cm^{-1} \cdot V^{-1}$, similar to the previous report [22]. However, the Stark tuning rate of $Na^+ \cdot H_2O$ on Mo_2C-PtO-2 is as high as 44.1 ± 1.8 $cm^{-1} \cdot V^{-1}$. Without PtO clusters decoration, the Stark tuning rate decreases to 11.4 ± 0.4 $cm^{-1} \cdot V^{-1}$ on bare 2D Mo_2C. The results indicate that the Mo_2C-PtO interfaces undergo more pronounced interactions with interfacial hydrated water molecules compared to Mo_2C and Pt/C. This phenomenon can be attributed to the electrostatic interactions at the interface between the $Na^+ \cdot H_2O$ hydrated cation and Mo_2C-PtO interfaces with rich electron aggregation, resulting in rapid migration of hydrated water from the outer Helmholtz layer into the inner Helmholtz layer, enhancing HER for closer proximity between free water molecules and Mo_2C-PtO interfaces, compared to 4-coordinated and 2-coordinated hydrogen-bonded water.

Density-functional theory (DFT) calculations are performed to analyze the enhanced HER activity of Mo_2C-PtO in alkaline media. A PtO cluster, comprising four Pt and four O atoms, is modeled on the Mo_2C

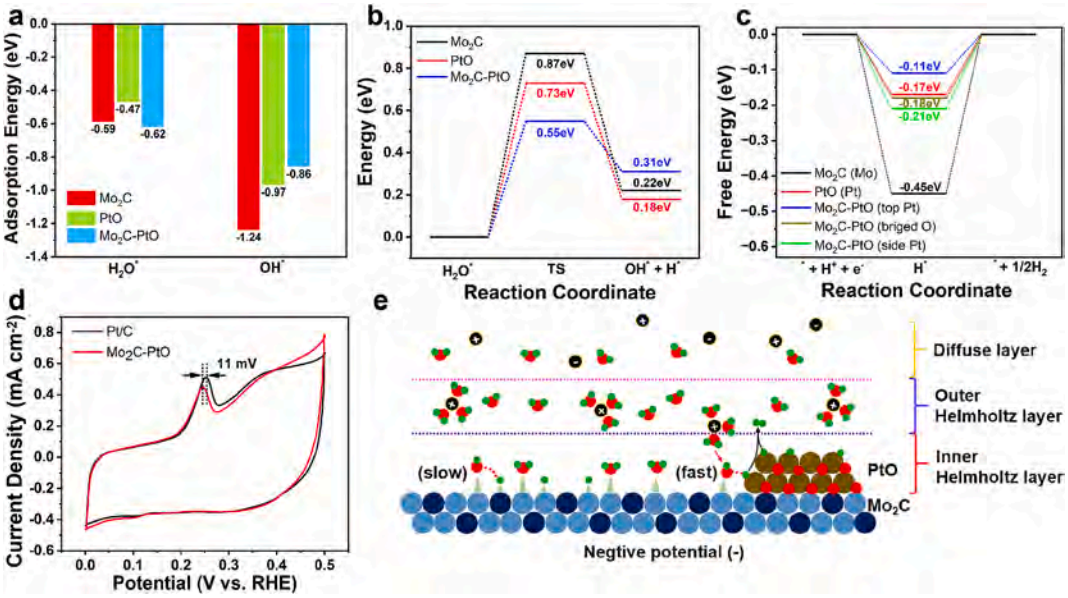

Fig. 5. (a) Computed binding energies of H_2O* and OH* of 2D Mo_2C, Mo_2C-PtO, and PtO; (b) Calculated energy barriers for water dissociation; (c) H*-adsorption free energy; (d) Cyclic voltammograms of Mo_2C-PtO in the non-Faraday zone in 1 M KOH compared to Pt/C; (e) Schematical illustration of HER mechanism of Mo_2C-PtO catalyst in alkaline media.

(101) surface (Fig. S22). Initially, an H_2O molecule adsorbs and then dissociates into OH* and H*. Fig. 5a shows that Mo_2C-PtO has a water adsorption energy of −0.62 eV, which is higher than those of Mo_2C (−0.59 eV) and PtO (−0.47 eV). Moreover, Mo_2C-PtO has a lower OH* adsorption energy of −0.86 eV compared to PtO (−0.97 eV) and Mo_2C (−1.24 eV), implying preferential adsorption of H_2O molecules at the Mo_2C-PtO interface, rapid OH* transfer to Mo_2C substrate, and freeing up more interfacial sites for water adsorption (Fig. S23). Fig. 5b shows the thermodynamics of H_2O splitting. The endothermic process of H_2O dissociation has an energy barrier of 0.55 eV at Mo_2C-PtO interface (Mo site), which is lower than those of Mo_2C (0.87 eV at Mo site) and PtO (0.73 eV at Pt site), suggesting easier H_2O dissociation at the Mo_2C-PtO interface. In the subsequent step, the relative free energy of H* adsorption at the active site is crucial to the catalytic activity. The Pt sites typically act as proton acceptors with the optimal H* adsorption energy to facilitate H_2 evolution. Fig. 5c indicates that ΔG for H* adsorption at top Pt sites of Mo_2C-PtO is approximately −0.11 eV, which is lower than that of the side Pt sites (−0.21 eV) and bridged O site (−0.18 eV), PtO surface (−0.17 eV at Pt sites), and Mo_2C (−0.45 eV at Mo sites), suggesting a potential rapid H* spillover from the interfacial site to the top Pt site during H_2 desorption (Fig. S24). The rapid hydrogen desorption mechanism on Mo_2C-PtO is further supported by the 11 mV negative shift in the hydrogen adsorption/desorption peak relative to the Pt/C catalyst (Fig. 5d) [52,53]. Based on the experimental results and theoretical calculations, the results reveal the catalytic behavior of interfacial water and hydrogen production at the Mo_2C-PtO interfaces at negative potentials, as shown in Fig. 5e. Cationic hydrated water penetrates the inner Helmholtz layer and is attracted by strong electrostatic interactions to the Mo_2C-PtO interfaces. The interface has high water adsorption energy and low dissociation energy, thus promoting the Volmer step and increasing the density of H* and OH* in the vicinity. The hydrated cation acts as a carrier to continuously supply free water in proximity to the interface, thereby enhancing electron transfer between free water and the electrode. Owing to the different adsorption energies, OH* preferentially adsorbs on Mo_2C, while H* accumulates on PtO surface and rapidly migrates and desorbs at top Pt sites. This process significantly enhances the alkaline HER activity of Mo_2C-PtO by facilitating a kinetically favorable Volmer-Tafel pathway.

To assess the feasibility of the Mo_2C-PtO catalyst for large-scale hydrogen production, an AEM electrolyzer is assembled with optimal Mo_2C-PtO as the cathode and a NiFe LDH-coated Ni foam electrode as the anode (Fig. 6a and Fig. S25). The NiFe LDH nanosheets are fabricated on the Ni foam electrode (Fig. S26). The steady-state polarization curve of the AEM electrolyzer comprising the Mo_2C-PtO-2 cathode and NiFe LDH anode delivers superior catalytic performance compared to the cell with the commercial 20 wt% Pt/C cathode and the same NiFe LDH anode (Fig. 6b). Specifically, the AEM electrolyzer (Mo_2C-PtO-2 || NiFe LDH) requires a cell voltage of only 2.05 V to achieve a current density of 1 A cm^{-2} at room temperature, thus outperforming the Pt/C || NiFe LDH cell (2.12 V@1 A cm^{-2}). The long-term stability is presented in Fig. 6c. Remarkably, the Mo_2C-PtO-2-based cell maintains exceptional stability at 0.5 A cm^{-2} for 100 h at room temperature without degradation. All in all, the Mo_2C-PtO catalyst with 0.98 wt% Pt has immense potential in industrial hydrogen production.

4. Conclusions

In summary, we have developed PtO nanoclusters modified ultrathin 2D Mo_2C (Mo_2C-PtO) catalyst with a Pt concentration of 0.98 wt% using a scalable and simple method. The 2D Mo_2C with a large surface area and abundant dangling bonds provides strong support for PtO catalysts. Our research reveals significant interfacial electronic interactions and strong electrostatic effects at the Mo_2C-PtO interface, confirmed by *in-situ* Raman spectroscopy and DFT calculations, leading to efficient hydrogen production in alkaline conditions via a rapid Volmer-Tafel mechanism. First, the differing work functions promote electron transfer from Mo_2C to PtO, leading to electron accumulation at the interface, which attracts hydrated cations to nearby active sites. Additionally, the

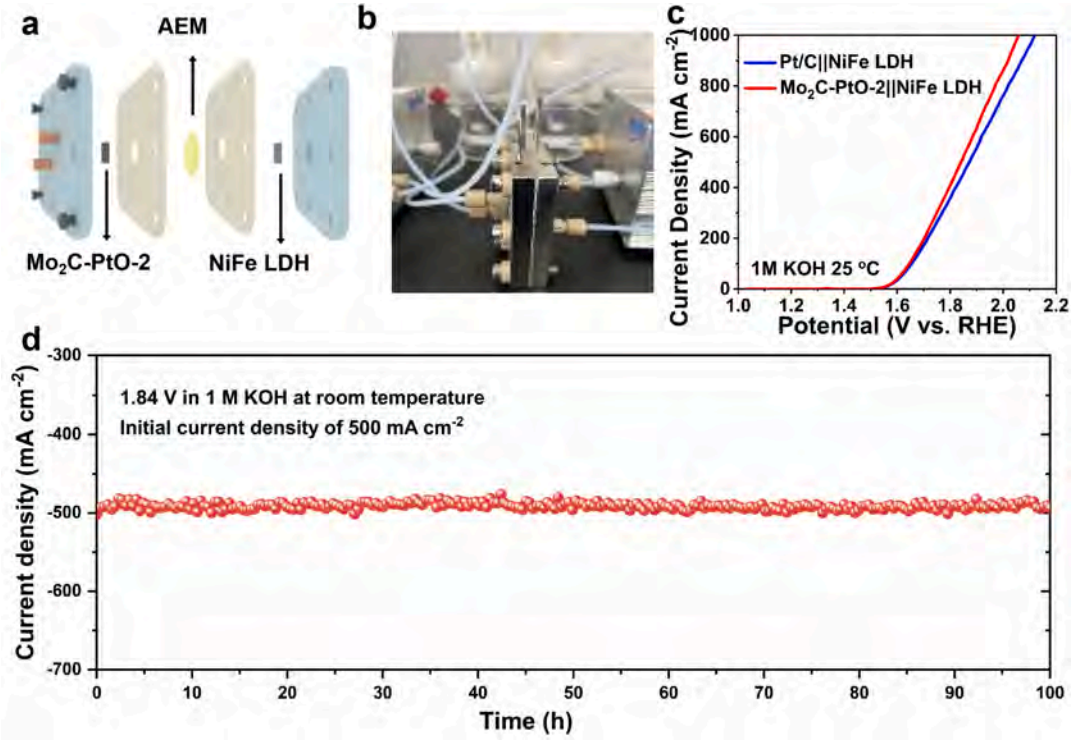

Fig. 6. (a) Schematic illustration and (b) Photograph of the AEM–WE apparatus comprising the Mo_2C-PtO-2 cathode and NiFe LDH anode; (c) I-V curves of AEM–WE with Mo_2C-PtO-2 or commercial 20 wt% Pt/C as the anode and NiFe LDH on Ni foam as the cathode at room temperature and ambient pressure; (d) Chronoamperometry testing of AEM-WE with Mo_2C-PtO-2 as the cathode at 1.84 V (initial current density of 500 mA cm^{-2}) at room temperature and ambient pressure.

optimized electronic structure favors the adsorption of key intermediates, OH* on Mo_2C and H* on PtO, increasing the availability of active sites at the interface. Consequently, the Mo_2C-PtO catalyst achieves a remarkably low overpotential of 5 mV at 10 mA cm^{-2}, a minimal Tafel slope of 24 mV dec^{-1}, and demonstrates excellent stability in alkaline electrolyte, outperforming commercial Pt/C catalysts in AEM devices. This study emphasizes the role of ionic hydrated water at the catalyst surface, providing valuable insights for the design of advanced catalysts with superior alkaline HER properties.

CRediT authorship contribution statement

Lei Xiang: Writing – original draft, Methodology, Investigation. **Difei Leng:** Visualization, Software. **Xuming Zhang:** Writing – review & editing, Writing – original draft, Resources, Project administration, Conceptualization. **Han Li:** Visualization, Methodology. **Handu Wang:** Visualization, Methodology. **Chaoran Pi:** Writing – original draft, Visualization, Investigation, Formal analysis, Data curation. **Shuangjie Wu:** Resources. **Li Huang:** Resources. **Yun Li:** Resources. **Kaifu Huo:** Writing – review & editing, Visualization. **Paul K. Chu:** Writing – review & editing, Visualization.

Declaration of competing interest

The authors declare that they have no known competing financial interests or personal relationships that could have appeared to influence the work reported in this paper.

Acknowledgments

This work was financially supported by the National Natural Science Foundation of China (22379116), and City University of Hong Kong Donation Research Grants (DON-RMG 9229021 and 9229021). The authors are grateful for the facility support provided by the Analytical & Testing Center of Wuhan University of Science and Technology.

Appendix A. Supplementary data

Supplementary data to this article can be found online at https://doi.org/10.1016/j.jcis.2025.02.103.

Data availability

Data will be made available on request.

References

[1] J. Zhu, L. Hu, P. Zhao, L. Lee, K. Wong, Recent advances in electrocatalytic hydrogen evolution using nanoparticles, Chem. Rev. 120 (2019) 851–918.
[2] Y. Yang, P. Li, X. Zheng, W. Sun, S. Dou, T. Ma, H. Pan, Anion-exchange membrane water electrolyzers and fuel cells, Chem. Soc. Rev. 51 (2022) 9620–9693.
[3] D. Li, A. Motz, C. Bae, C. Fujimoto, G. Yang, F. Zhang, K. Ayers, Y. Kim, Durability of anion exchange membrane water electrolyzers, Energ. Environ. Sci. 14 (2021) 3393–3419.
[4] D. Strmcnik, P. Lopes, B. Genorio, V. Stamenkovic, N. Markovic, Design principles for hydrogen evolution reaction catalyst materials, Nano Energy 29 (2016) 29–36.
[5] W. Sheng, H. Gasteiger, Y. Horn, Hydrogen oxidation and evolution reaction kinetics on platinum: acid vs alkaline electrolytes, J. Electrochem. Soc. 157 (2010) B1529.
[6] X. Chen, X. Wang, J. Le, S. Li, X. Wang, Y. Zhang, P. Radjenovic, Y. Zhao, Y. Wang, X. Lin, J. Dong, J. Li, Revealing the role of interfacial water and key intermediates at ruthenium surfaces in the alkaline hydrogen evolution reaction, Nat. Commun. 14 (2023) 5289.
[7] W. Ma, X. Zhang, W. Li, M. Jiao, L. Zhang, R. Ma, Z. Zhou, Advanced Pt-based electrocatalysts for the hydrogen evolution reaction in alkaline medium, Nanoscale 15 (2023) 11759–11776.
[8] Z. Li, R. Ge, J. Su, L. Chen, Recent progress in low Pt content electrocatalysts for hydrogen evolution reaction, Adv. Mater. Inter., 7 (2020) 2000396.
[9] H. Zeng, Y. Ji, J. Wen, X. Li, T. Zheng, Q. Jiang, C. Xia, Pt nanocluster-catalyzed hydrogen evolution reaction: Recent advances and future outlook, Chinese Chem. Lett., 109686 (2024).
[10] Y. Wang, W. Wu, R. Chen, C. Lin, S. Mu, N. Cheng, Reduced water dissociation barrier on constructing Pt-Co/CoO_x interface for alkaline hydrogen evolution, Nano Res. 15 (2022) 4958–4964.
[11] N. Cheng, S. Stambula, D. Wang, M. Banis, J. Liu, A. Riese, B. Xiao, R. Li, T. Sham, L. Liu, G. Botton, X. Sun, Platinum single-atom and cluster catalysis of the hydrogen evolution reaction, Nat. Commun. 7 (2016) 13638.
[12] J. Chen, M. Aliasgar, F. Zamudio, T. Zhang, Y. Zhao, X. Lian, L. Wen, H. Yang, W. Sun, S. Kozlov, W. Chen, L. Wang, Diversity of platinum-sites at platinum/fullerene interface accelerates alkaline hydrogen evolution, Nat. Commun. 14 (2023) 1711.
[13] G. Gao, G. Zhu, X. Chen, Z. Sun, A. Cabot, Optimizing Pt-based alloy electrocatalysts for improved hydrogen evolution performance in alkaline electrolytes: a comprehensive review, ACS Nano 17 (2023) 20804–20824.
[14] F. Yu, Z. Lang, L. Yin, K. Feng, Y. Xia, H. Tan, H. Zhu, J. Zhong, Z. Kang, Y. Li, Pt-O bond as an active site superior to Pt^0 in hydrogen evolution reaction, Nat. Commun. 11 (2020) 490.
[15] X. Cheng, Y. Li, L. Zheng, Y. Yan, Y. Zhang, G. Chen, S. Sun, J. Zhang, Highly active, stable oxidized platinum clusters as electrocatalysts for the hydrogen evolution reaction, Energ. Environ. Sci. 10 (2017) 2450–2458.
[16] K. Feng, H. Zheng, D. Zhang, G. Yuan, L. Chang, Y. Chen, J. Zhong, Carbon nanotube supported PtO_x nanoparticles with hybrid chemical states for efficient hydrogen evolution, J. Energy. Chem., 58 (2021) 364–369.
[17] Y. Zhao, P. Kumar, X. Tan, X. Lu, X. Zhu, J. Jiang, J. Pan, S. Xi, H. Yang, Z. Ma, T. Wan, D. Chu, W. Jiang, S. Smith, R. Amal, Z. Han, X. Lu, Modulating Pt-O-Pt atomic clusters with isolated cobalt atoms for enhanced hydrogen evolution catalysis, Nat. Commun. 13 (2022) 2430.
[18] H. Yang, Y. Ji, Q. Shao, W. Zhu, M. Fang, M. Ma, F. Liao, H. Huang, Y. Zhang, J. Yang, Z. Fan, Y. Li, Y. Liu, M. Shao, Z. Kang, Metastable-phase platinum oxide for clarifying the Pt-O active site for the hydrogen evolution reaction, Energ. Environ. Sci. 16 (2023) 574–583.
[19] S. Ramakrishnan, S. Vijayapradeep, S. Selvaraj, J. Huang, S. Karthikeyan, R. Gutru, N. Logeshwaran, T. Miyazaki, M. Mamlouk, D. Yoo, An efficient cathode electrocatalyst for anion exchange membrane water electrolyzer, Carbon 220 (2024) 118816.
[20] J. Wu, J. Su, T. Wu, L. Huang, Q. Li, Y. Luo, H. Jin, J. Zhou, T. Zhai, D. Wang, Y. Gogotsi, Y. Li, Scalable synthesis of 2D Mo_2C and thickness-dependent hydrogen evolution on its basal plane and edges, Adv. Mater. 35 (2023) 2209954.
[21] D. Deng, K. Novoselov, Q. Fu, N. Zheng, Z. Tian, X. Bao, Catalysis with two-dimensional materials and their heterostructures, Nat. Nanotechnol. 11 (2016) 218–230.
[22] A. Shah, Z. Zhang, Z. Huang, S. Wang, G. Zhong, C. Wan, A. Alexandrova, Y. Huang, X. Duan, The role of alkali metal cations and platinum-surface hydroxyl in the alkaline hydrogen evolution reaction, Nat. Catal. 5 (2022) 923–933.
[23] J. Li, Z. Guo, W. Zhang, J. Guo, K. Qu, W. Cai, Stable NiPt-Mo_2C active site pairs enable boosted water splitting and direct methanol fuel cell, Green, Energy Environ. 8 (2023) 559–566.
[24] L. Xie, X. Ren, Q. Liu, G. Cui, R. Ge, A. Asiri, X. Sun, Q. Zhang, L. Chen, A $Ni(OH)_2$-PtO_2 hybrid nanosheet array with ultralow Pt loading toward efficient and durable alkaline hydrogen evolution, J. Mater. Chem. A 6 (2018) 1967–1970.
[25] D. Xiang, J. Bao, L. Zhang, P. Xin, C. Yue, A. Naseri, H. Wang, S. Huang, K. Uvdal, Z. Hu, Interfacial electronic structure modulations of Au@CuS with defective Ni-doped CoS_2 facilitates the electroreduction of N_2 into NH_3, Chem. Eng. J. 493 (2024) 152456.
[26] K. Wang, S. Wang, K. Hui, J. Li, C. Zha, D. Dinh, Z. Shao, B. Yan, Z. Tang, K. Hui, Dense platinum/nickel oxide heterointerfaces with abundant oxygen vacancies enable ampere-level current density ultrastable hydrogen evolution in alkaline, Adv. Funct. Mater. 33 (2022) 2211273.
[27] Z. Shi, X. Zhang, X. Lin, G. Liu, C. Ling, S. Xi, B. Chen, Y. Ge, C. Tan, Z. Lai, Z. Huang, X. Ruan, L. Zhai, L. Li, Z. Li, X. Wang, G. Nam, J. Liu, Q. He, Z. Guan, J. Wang, C. Lee, A. Kucernak, H. Zhang, Phase-dependent growth of Pt on MoS_2 for highly efficient H_2 evolution, Nature 621 (2023) 300–305.
[28] J. Sun, W. Xu, C. Lv, L. Zhang, M. Shakouri, Y. Peng, Q. Wang, X. Yang, D. Yuan, M. Huang, Y. Hu, D. Yang, L. Zhang, Co/MoN hetero-interface nanoflake array with enhanced water dissociation capability achieves the Pt-like hydrogen evolution catalytic performance, Appl. Catal. B Environ., 286 (2021) 119882.
[29] Y. Ye, Y. Shi, J. Cai, Z. Xiao, Z. Li, S. Lin, Mo_2C promoted electrocatalysis of the Pt/Mo_2C heterostructure for a superior hydrogen evolution reaction, Dalton T. 52 (2023) 3682–3689.
[30] X. Zhang, M. Zhang, Y. Deng, M. Xu, L. Artiglia, W. Wen, R. Gao, B. Chen, S. Yao, X. Zhang, M. Peng, J. Yan, A. Li, Z. Jiang, X. Gao, S. Cao, C. Yang, A.J. Kropf, J. Shi, J. Xie, M. Bi, J. Bokhoven, Y. Li, X. Wen, M. Stephanopoulos, C. Shi, W. Zhou, D. Ma, A stable low-temperature H_2-production catalyst by crowding Pt on α-MoC, Nature 589 (2021) 396–401.
[31] Y. Ma, G. Guan, X. Hao, J. Cao, A. Abudula, Molybdenum carbide as alternative catalyst for hydrogen production-A review, Renew. Sust. Energy Rev., 75 (2017) 1101–1129.
[32] A. Huang, H. Huang, F. Wang, N. Ke, C. Tan, L. Hao, X. Xu, Y. Xian, S. Agathopoulos, Mo_2C-based ceramic electrode with high stability and catalytic activity for hydrogen evolution reaction at high current density, Small 20 (2024) 2308068.
[33] M. Qiang, X. Zhang, H. Song, C. Pi, X. Wang, B. Gao, Y. Zheng, X. Peng, P. Chu, K. Huo, General synthesis of nanostructured Mo_2C electrocatalysts using a carbon template for electrocatalytic applications, Carbon 197 (2022) 238–245.
[34] J. Fang, H. Wang, Q. Dang, H. Wang, X. Wang, J. Pei, Z. Xu, C. Chen, W. Zhu, H. Li, Y. Yan, Z. Zhuang, Atomically dispersed Iridium on Mo_2C as an efficient and stable alkaline hydrogen oxidation reaction catalyst, Nat. Commun. 15 (2024) 4236.

[35] L. Zhang, T. Yang, W. Zang, Z. Kou, Y. Ma, M. Waqar, X. Liu, L. Zheng, S. Pennycook, Z. Liu, X. Loh, L. Shen, J. Wang, Quasi-paired Pt atomic sites on Mo_2C promoting selective four-electron oxygen reduction, Adv. Sci. 8 (2021) 2101344.
[36] V. Do, Y. Li, P. Prabhu, W. Xie, P. Kidkhunthod, H. Wang, G. Wang, J. Lee, Surface confinement of atomically thin Pt nanoclusters on 2D δ-Mon for durable pH-universal hydrogen evolution, Adv. Funct. Mater. 33 (2023) 2302297.
[37] S. Huang, J. Bao, D. Xiang, C. Gao, K. Peng, Q. Chen, S. Ma, Y. Jiang, Z. Hu, J. Zhang, Enhancing electroreduction activity and selectivity of N_2-to-NH_3 through proton-feeding adjustments in Ag@AgP_2@Ni-CoP@C core-shell nanowires, Appl. Catal. B Environ. 337 (2023) 122998.
[38] Q. Xu, J. Zhang, H. Zhang, L. Zhang, L. Chen, Y. Hu, H. Jiang, C. Li, Atomic heterointerface engineering overcomes the activity limitation of electrocatalysts and promises highly-efficient alkaline water splitting, Energ. Environ. Sci. 14 (2021) 5228–5259.
[39] N. Danilovic, R. Subbaraman, D. Strmcnik, K. Chang, A. Paulikas, V. Stamenkovic, N. Markovic, Enhancing the alkaline hydrogen evolution reaction activity through the bifunctionality of $Ni(OH)_2$/metal catalysts, Angew. Chem. Inte. Ed., 51 (2012) 12495–12498.
[40] T. Kühne, M. Iannuzzi, M. Ben, V. Rybkin, P. Seewald, F. Stein, T. Laino, R. Khaliullin, O. Schütt, F.P. Schiffmann, CP2K: An electronic structure and molecular dynamics software package-quickstep: efficient and accurate electronic structure calculations, J. Chem. Phys. 152 (2020) 194103.
[41] T. Lu, Q. Chen, Shermo: A general code for calculating molecular thermochemistry properties, Comput. Theor. Chem. 1200 (2021) 113249.
[42] C. Wang, X. Li, H. Song, P.K. Chu, K. Huo, In-plane heterostructured MoN/MoC nanosheets with enhanced interfacial charge transfer for superior pseudocapacitive storage, Adv. Funct. Mater. 34 (2024) 2311040.
[43] C. Wang, H. Fan, X. Ren, Y. Wen, W. Wang, Highly dispersed PtO nanodots as efficient co-catalyst for photocatalytic hydrogen evolution, Appl. Surf. Sci. 462 (2018) 423–431.
[44] P. Nguyen, Q. Dao, T. Dang, T. Hoang, J. Chung, E. Shin, Highly dispersed PtO over g-C_3N_4 by specific metal-support interactions and optimally distributed Pt species to enhance hydrogen evolution rate of Pt/g- C_3N_4 photocatalysts, Chem. Eng. J. 464 (2023) 142765.
[45] H. Yan, Y. Xie, Y. Jiao, A. Wu, C. Tian, X. Zhang, L. Wang, H. Fu, Holey reduced graphene oxide coupled with an Mo_2N-Mo_2C heterojunction for efficient hydrogen evolution, Adv. Mater. 30 (2018) 1704156.
[46] P. Lamoureux, A. Singh, K. Chan, pH effects on hydrogen evolution and oxidation over Pt(111): insights from frst-principles, ACS Catal. 9 (2019) 6194–6201.
[47] L. Chen, Q. Xu, S. Oener, K. Fabrizio, S. Boettcher, Design principles for water dissociation catalysts in high-performance bipolar membranes, Nat. Commun. 13 (2022) 3846.
[48] J. Li, Y. Huang, S. Duan, R. Pang, D. Wu, B. Ren, X. Xu, Z. Tian, SERS and DFT study of water on metal cathodes of silver, gold and platinum nanoparticles, PCCP 12 (2010) 2493–2502.
[49] H. Shi, T. Wang, J. Liu, W. Chen, S. Li, J. Liang, S. Liu, X. Liu, Z. Cai, C. Wang, A sodium-ion-conducted asymmetric electrolyzer to lower the operation voltage for direct seawater electrolysis, Nat. Commun. 14 (2023) 3934.
[50] L. Shen, B. Lu, Y. Li, J. Liu, Z. Huang, H. Peng, J. Ye, X. Qu, J. Zhang, G. Li, W. Cai, Y. Jiang, S. Sun, Interfacial structure of water as a new descriptor of the hydrogen evolution reaction, Angew. Chem. Int. Ed. 59 (2020) 22397–22402.
[51] Y. Wang, S. Zheng, W. Yang, R. Zhou, Q. He, P. Radjenovic, J. Dong, S. Li, J. Zheng, Z. Yang, G. Attard, F. Pan, Z. Tian, J. Li, In situ Raman spectroscopy reveals the structure and dissociation of interfacial water, Nature 600 (2021) 81–85.
[52] G. Zhao, L. Xia, P. Cui, Y. Qian, Y. Jiang, Y. Zhao, H. Pan, S. Dou, W. Sun, Atomic-level modulation of the interface chemistry of platinum-nickel oxide toward enhanced hydrogen electrocatalysis kinetics, Nano Lett. 21 (2021) 4845–4852.
[53] Y. Wang, G. Wang, G. Li, B. Huang, J. Pan, Q. Liu, J. Han, L. Xiao, J. Lu, L. Zhuang, Pt-Ru catalyzed hydrogen oxidation in alkaline media: oxophilic effect or electronic effect? Energ. Environ. Sci. 8 (2015) 177–181.

Supporting Information for

PtO Nanoclusters on Ultra-Thin 2D Mo_2C Enhance Hydrated Cation Interaction for Superior Alkaline Hydrogen Evolution Reaction

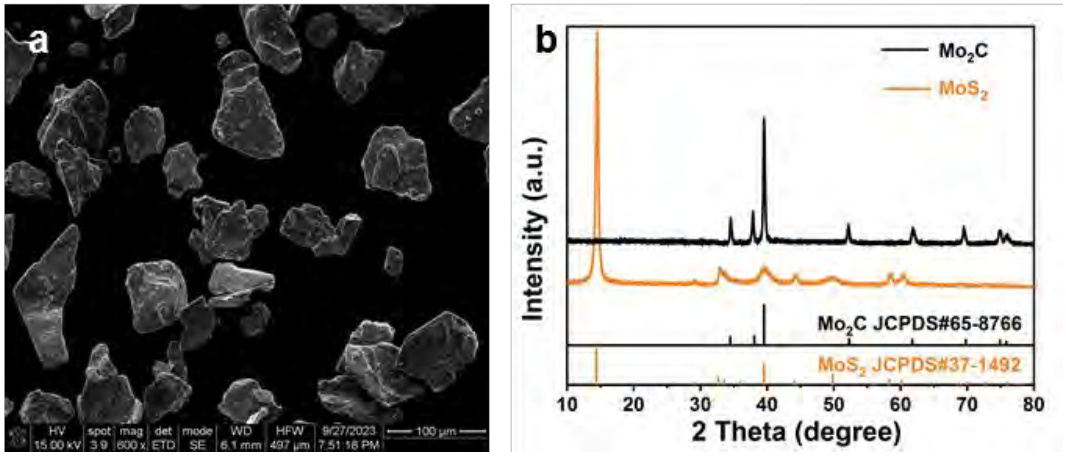

Figure S1 (a) SEM image of commercial MoS_2 powder; (b) XRD patterns of MoS_2 before and after molten salt treatment and subsequent washing.

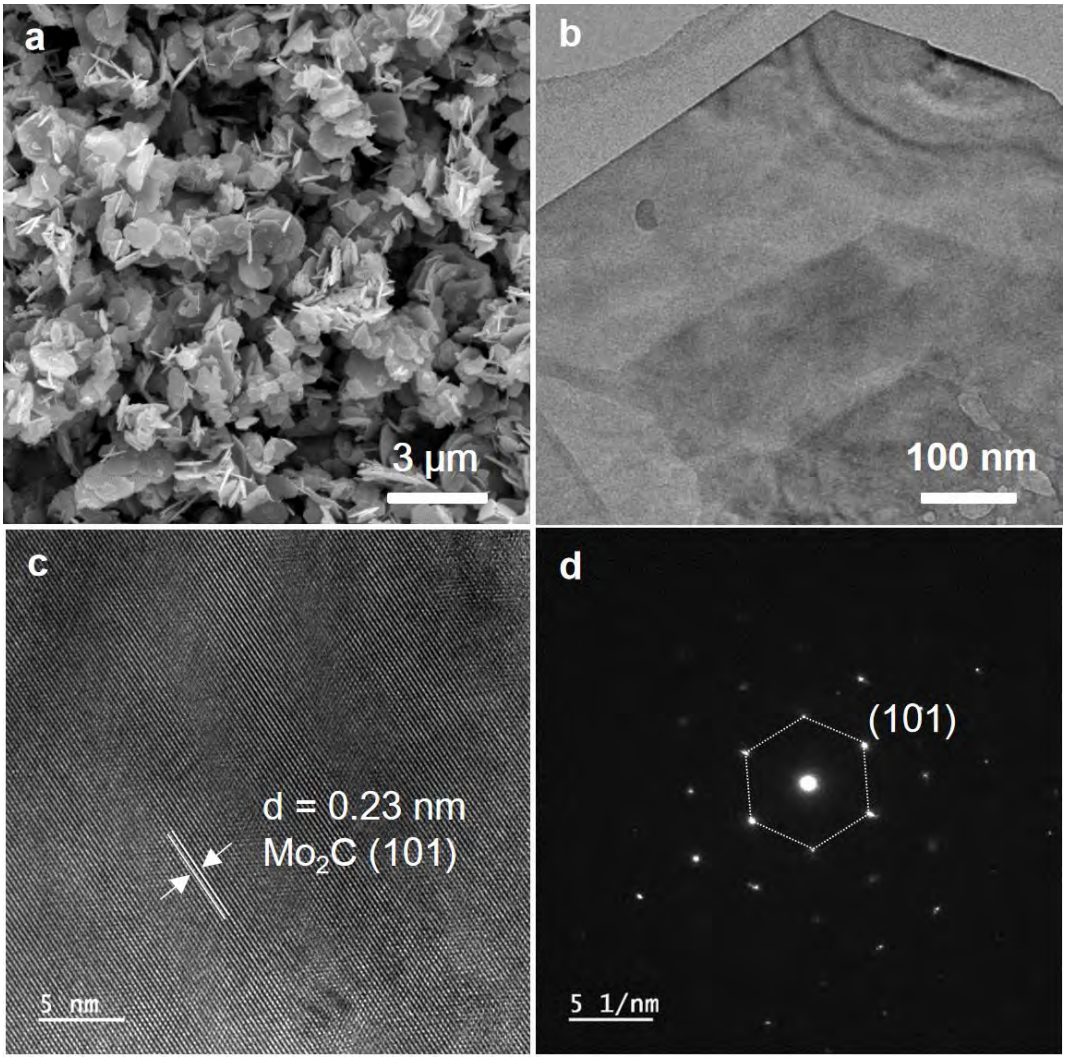

Figure S2 (a) SEM, (b) TEM and (c) HRTEM image of 2D Mo_2C; (d) Corresponding SAED pattern.

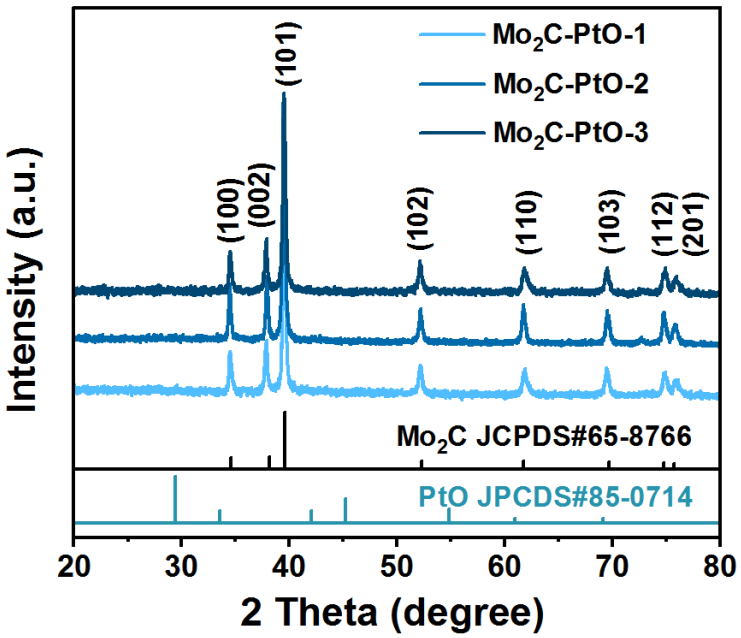

Figure S3 XRD patterns of 2D Mo_2C loaded with different PtO content.

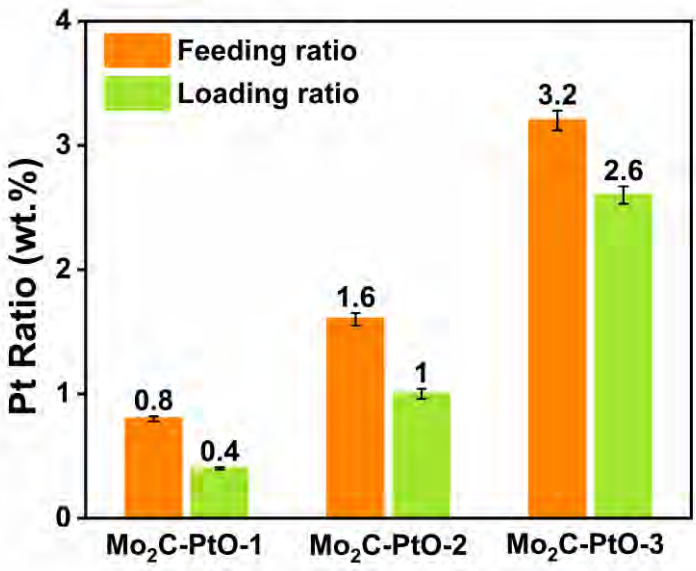

Figure S4 Pt feeding ratio (0.5 mg, 1 mg and 2 mg $H_2PtCl_6 \cdot 6H_2O$ in 25 mg of 2D Mo_2C powder) and loading ratio. (The error analysis was conducted after three measurements (n=3)).

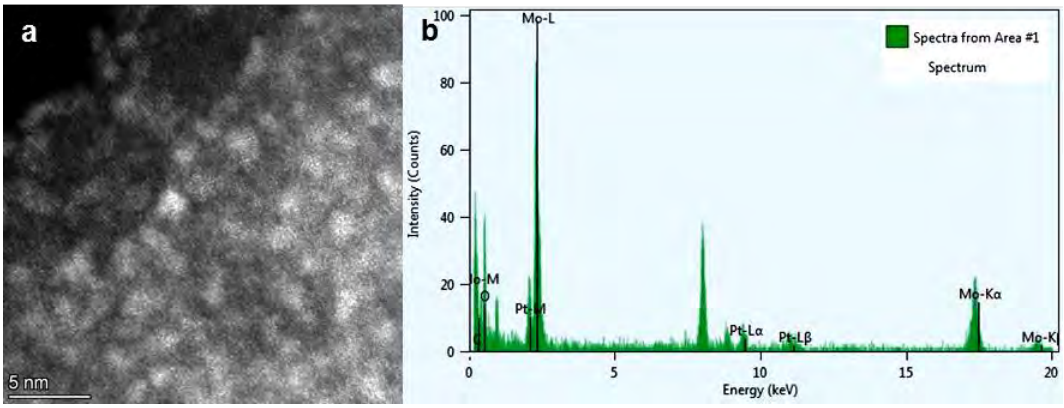

Figure S5 (a) HAADF-STEM image and (b) EDS spectra of Mo_2C-PtO-1.

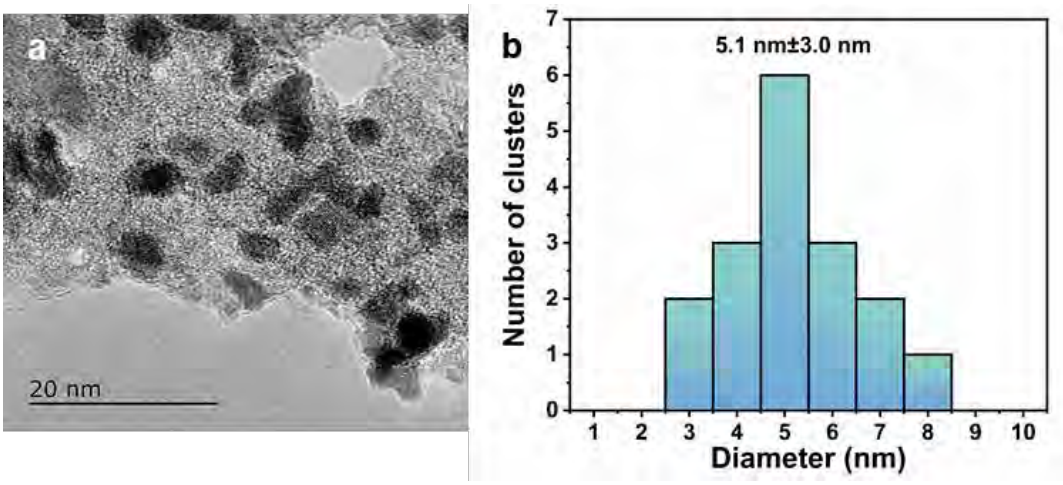

Figure S6 (a) TEM image of Mo_2C-PtO-3 and (b) corresponding size distribution of PtO clusters.

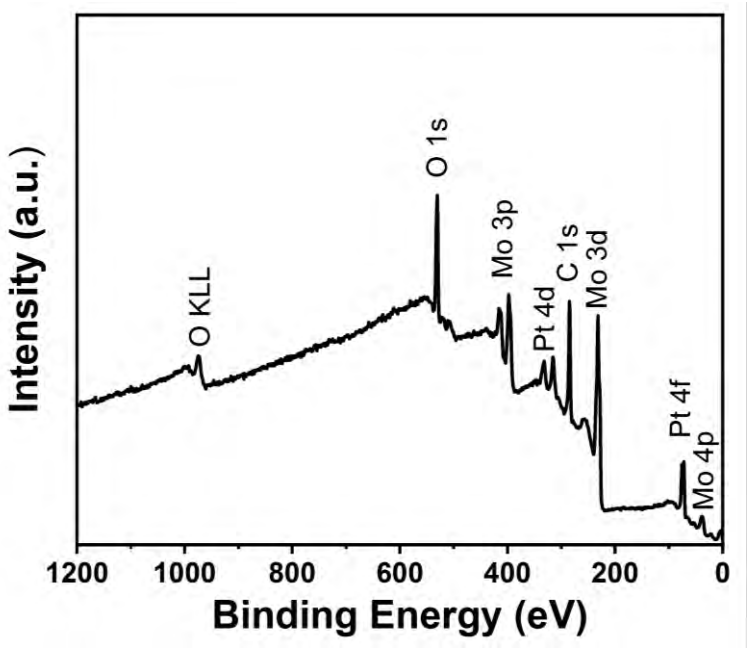

Figure S7 Full XPS spectra of Mo_2C-PtO-2.

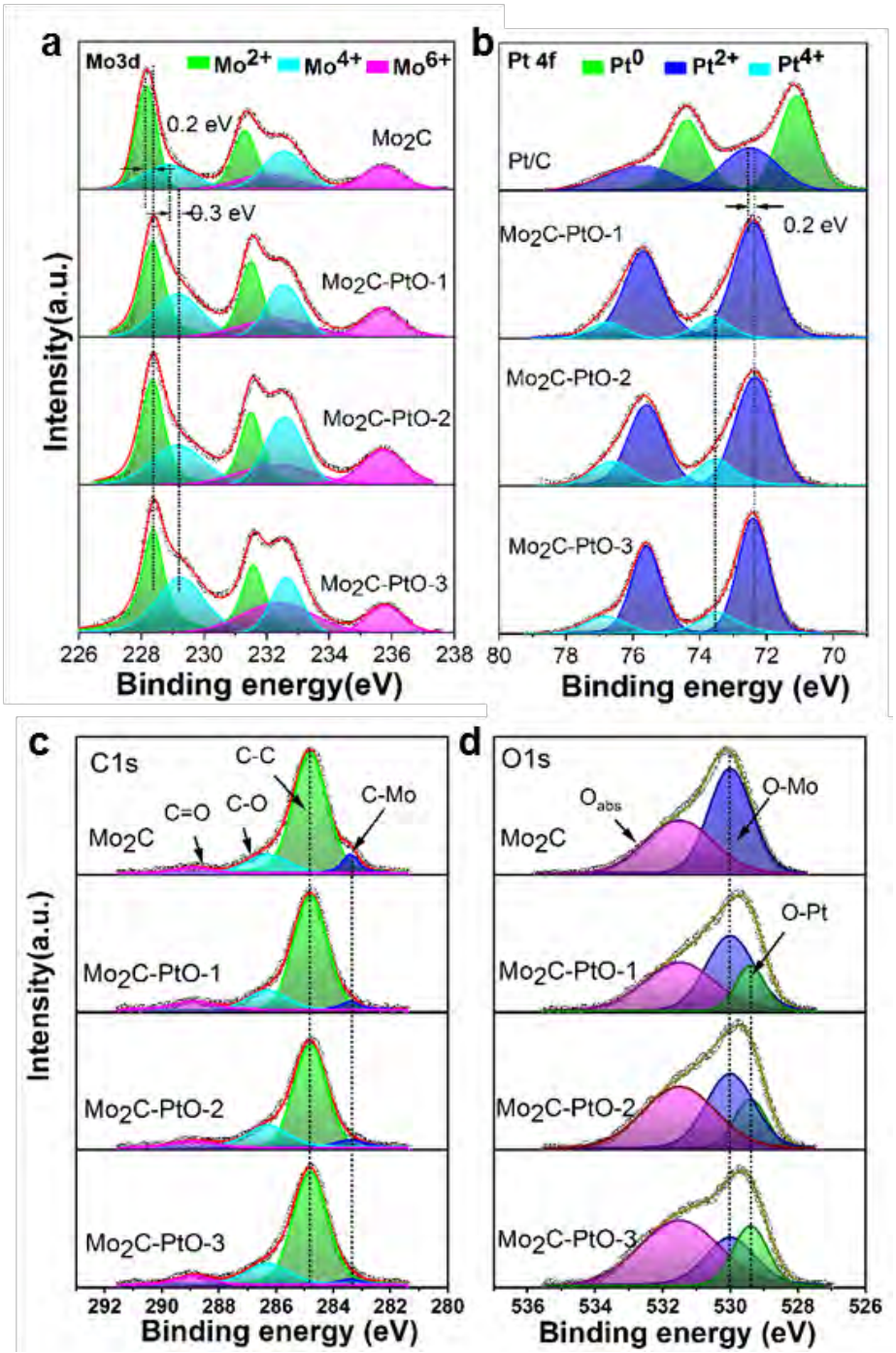

Figure S8 XPS spectrum of (a) Mo 3d, (b) Pt 4f, (c) C1s and (d) O1s of 2D Mo_2C, Mo_2C-PtO-1, Mo_2C-PtO-2, and Mo_2C-PtO-3.

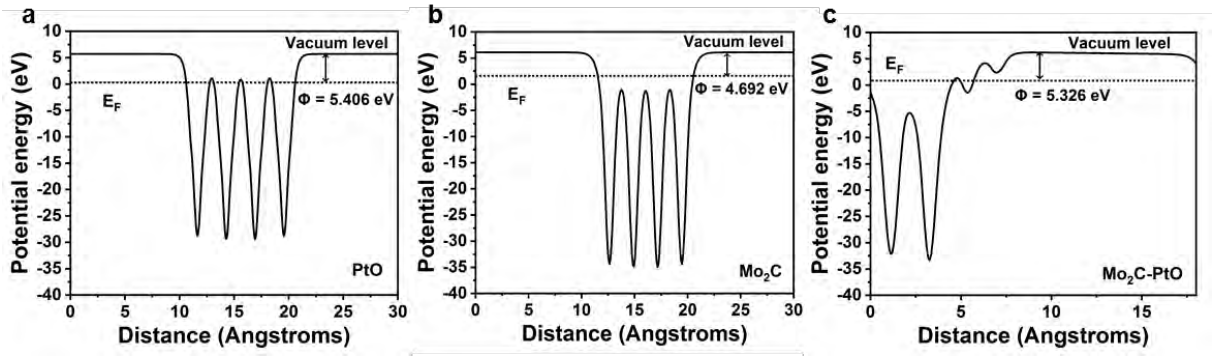

Figure S9 The work function of (a) PtO, (b) Mo_2C and (c) Mo_2C-PtO.

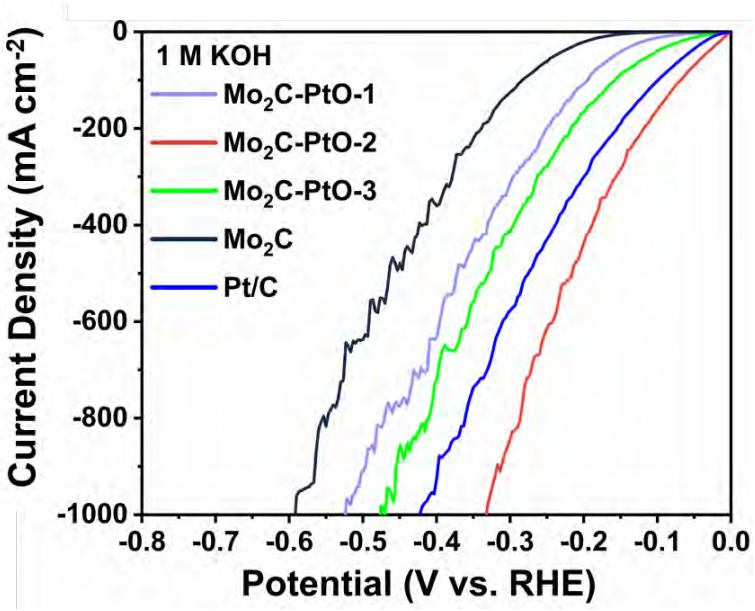

Figure S10 LSV curves of 2D Mo_2C, Mo_2C-PtO-1, Mo_2C-PtO-2, Mo_2C-PtO-3 and 20 wt.% Pt/C in 1 M KOH.

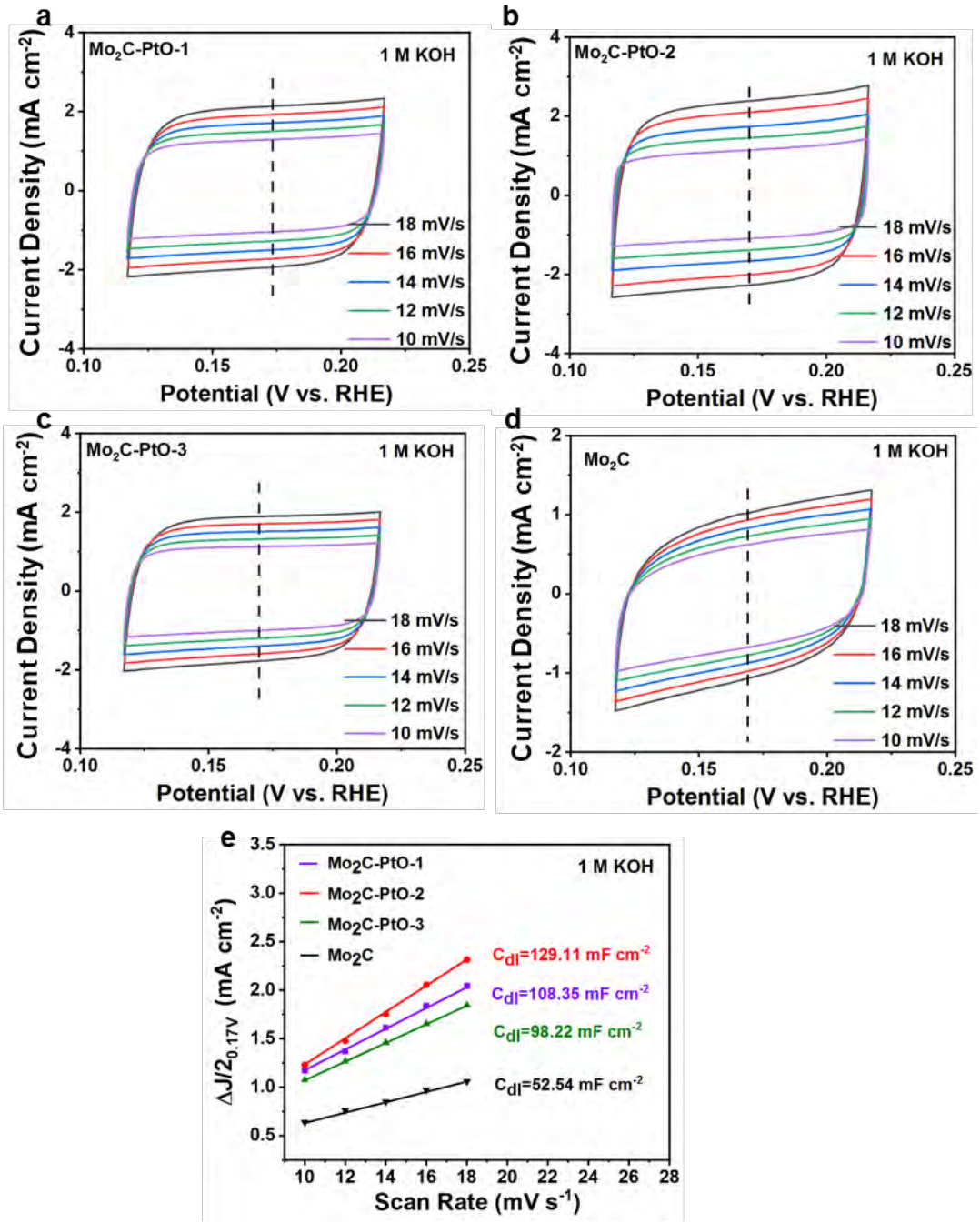

Figure S11 Cyclic voltammograms of (a) Mo_2C-PtO-1, (b) Mo_2C-PtO-2, (c) Mo_2C-PtO-3 and (d) Mo_2C in the region from -0.12 V to 0.22 V (vs. RHE) in 1 M KOH at different scan rates; (e) linear relationships between capacitive current and scan rate of these samples.

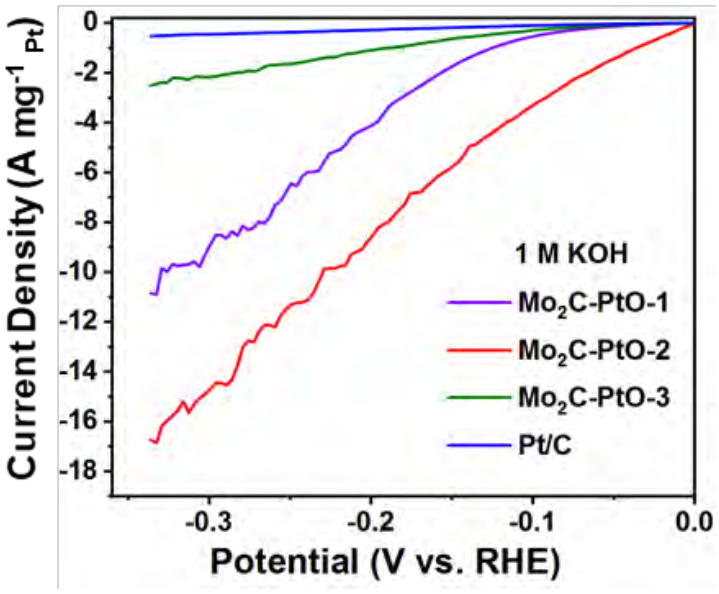

Figure S12 Mass activity of Pt in Mo_2C-PtO-1, Mo_2C-PtO-2 and Mo_2C-PtO-3 and 20% Pt/C in 1 M KOH.

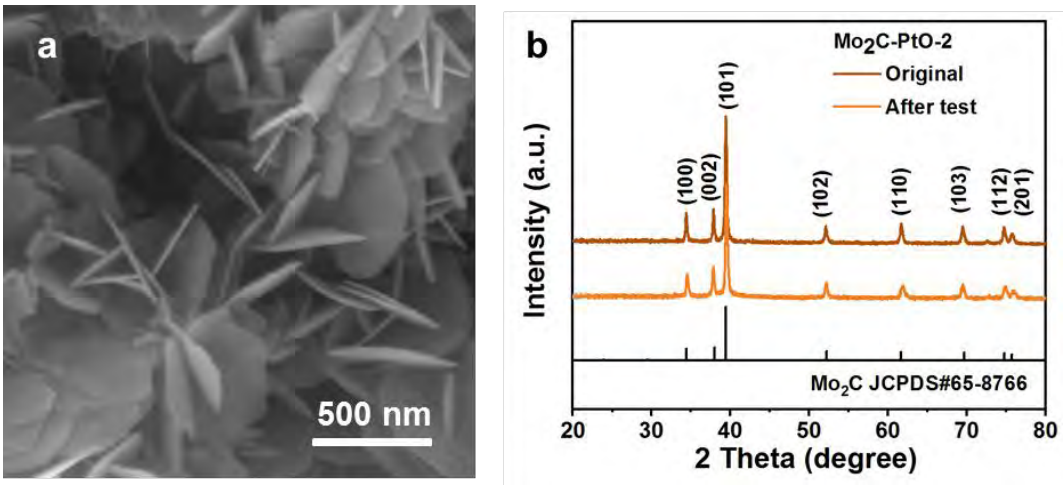

Figure S13 (a) SEM image and (b) XRD patterns of Mo_2C-PtO-2 catalyst after chronoamperometry testing for 300 h.

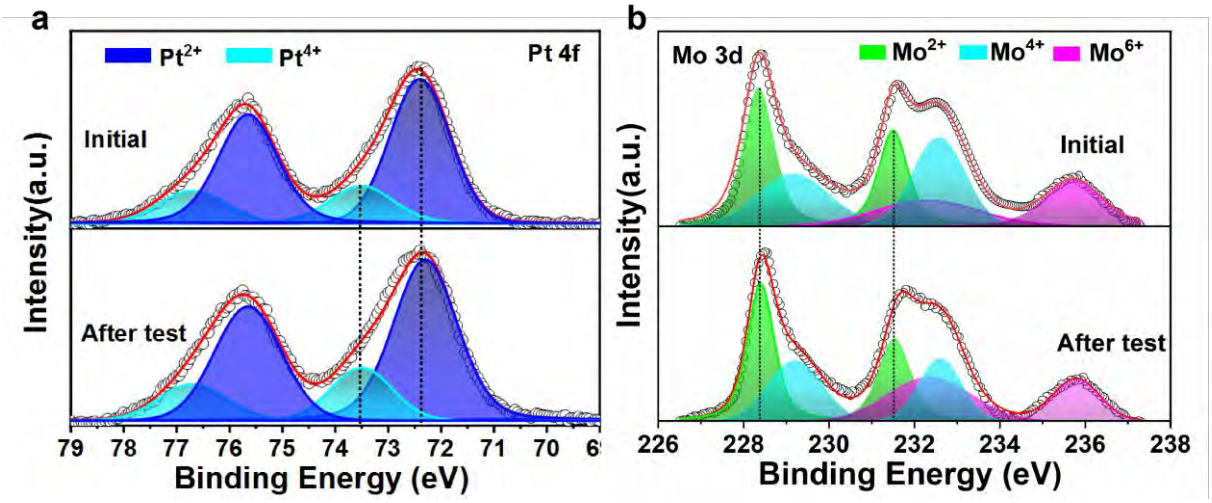

Figure S14 (a) Pt 4f and (b) Mo 3d XPS spectra of Mo_2C-PtO-2 before and after chronoamperometry testing for 300 h.

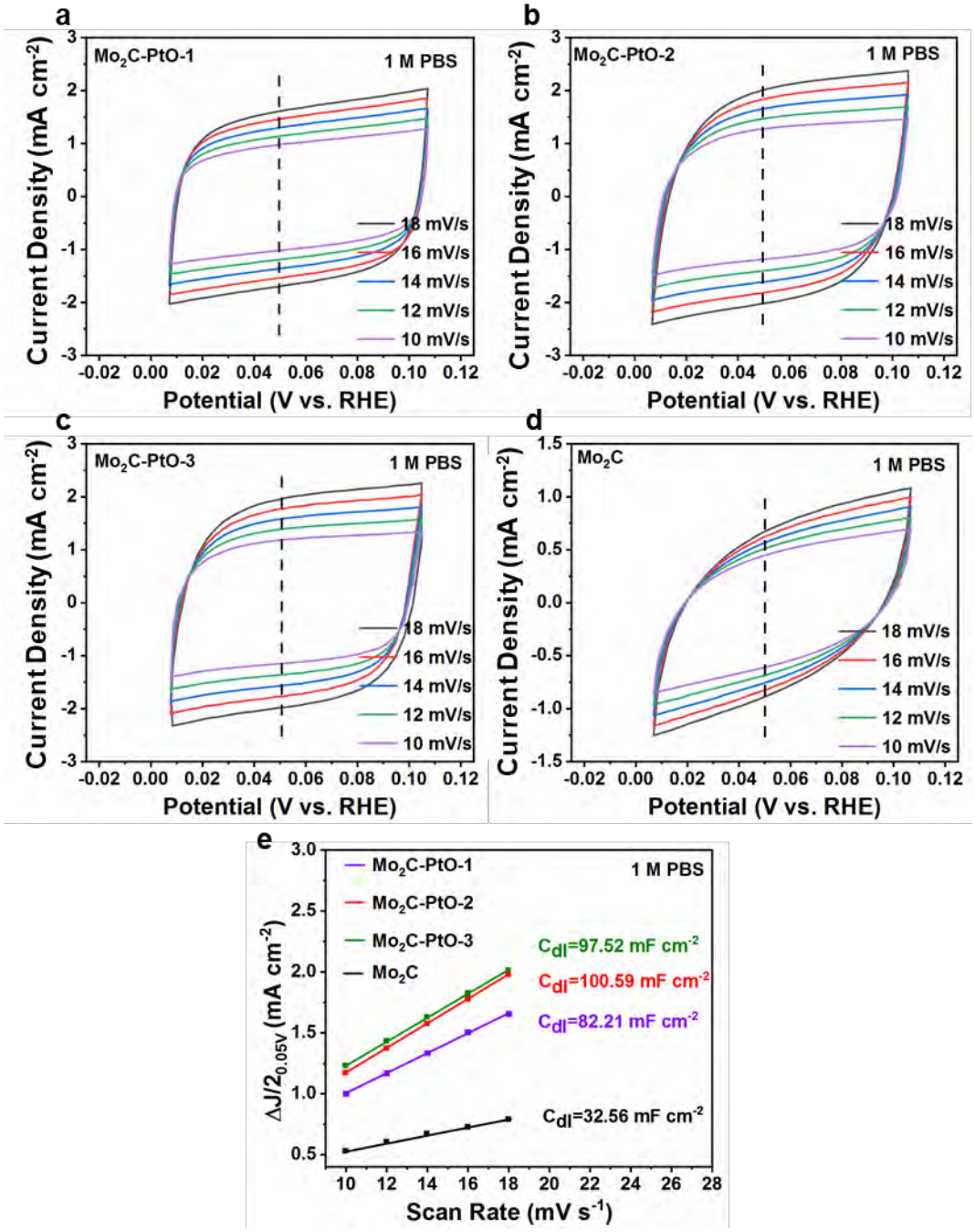

Figure S15 Cyclic voltammograms of (a) Mo_2C-PtO-1, (b) Mo_2C-PtO-2, (c) Mo_2C-PtO-3 and (d) Mo_2C in the region from -0.12 V to 0.22 V (vs. RHE) in 1 M PBS at different scan rates; (e) linear relationships between capacitive current and scan rate of these samples.

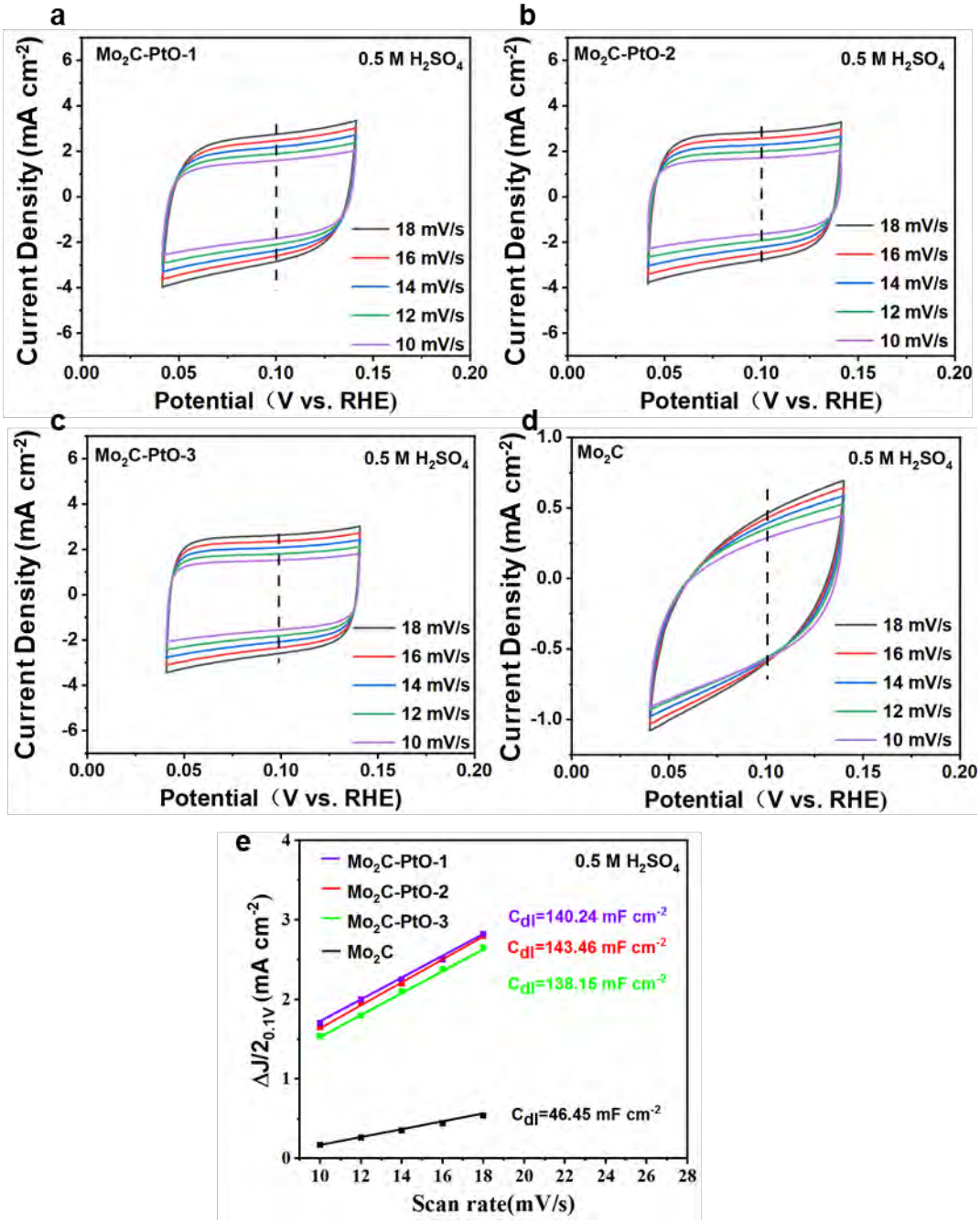

Figure S16 Cyclic voltammograms of (a) Mo_2C-PtO-1, (b) Mo_2C-PtO-2, (c) Mo_2C-PtO-3 and (d) Mo_2C in the region from -0.12 V to 0.22 V (vs. RHE) in 0.5 M H_2SO_4 at different scan rates; (e) linear relationships between capacitive current and scan rate of these samples.

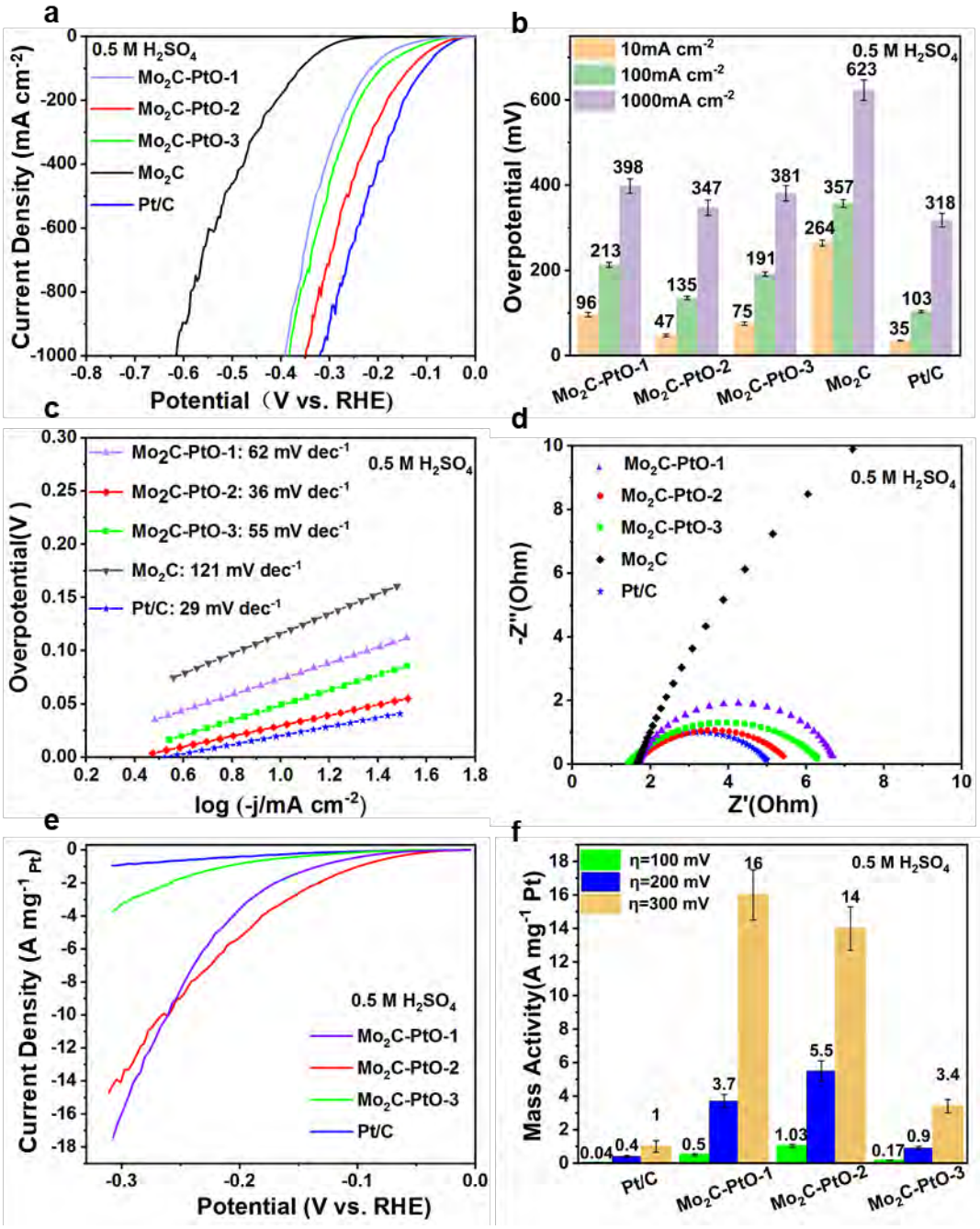

Figure S17 (a) The polarization curves of Mo_2C-PtO-1, Mo_2C-PtO-2 and Mo_2C-PtO-3, 2D Mo_2C and 20% Pt/C in 0.5 M H_2SO_4; (b) Corresponding overpotentials of samples at different current densities; (c) Tafel slope; (d) Nyquist plots; (e), (f) Mass activity of Pt in Mo_2C-PtO-1, Mo_2C-PtO-2 and Mo_2C-PtO-3 and 20% Pt/C. (The error analysis was conducted after three measurements (n=3)).

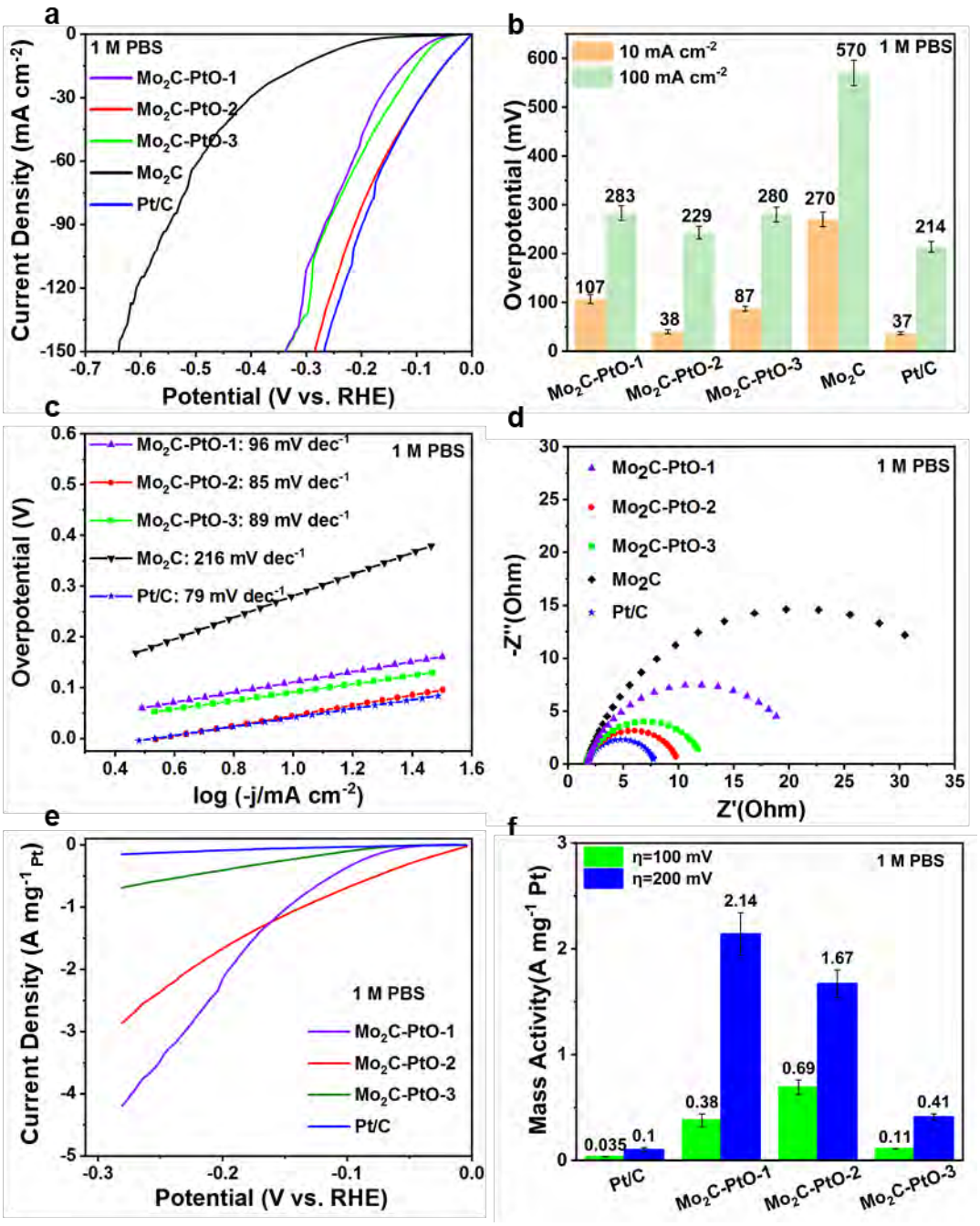

Figure S18 (a) The polarization curves of Mo_2C-PtO-1, Mo_2C-PtO-2 and Mo_2C-PtO-3, 2D Mo_2C and 20% Pt/C in 1 M PBS; (b) Corresponding overpotentials of samples at different current densities; (c) Tafel slope; (d) Nyquist plots; (e), (f) Mass activity of Pt in Mo_2C-PtO-1, Mo_2C-PtO-2 and Mo_2C-PtO-3 and 20% Pt/C. (The error analysis was conducted after three measurements (n=3)).

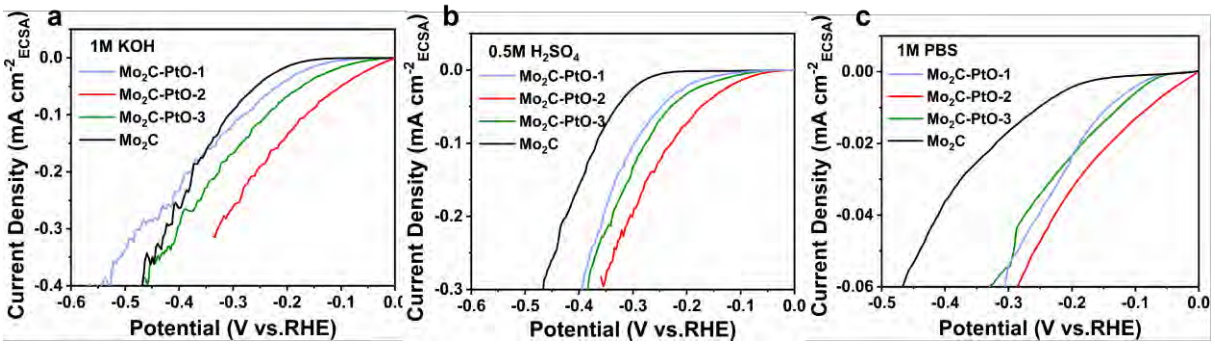

Figure S19 ECSA-normalized LSVs of Mo_2C-PtO-1, Mo_2C-PtO-2, Mo_2C-PtO-3 and Mo_2C in basic, acid and neutral media.

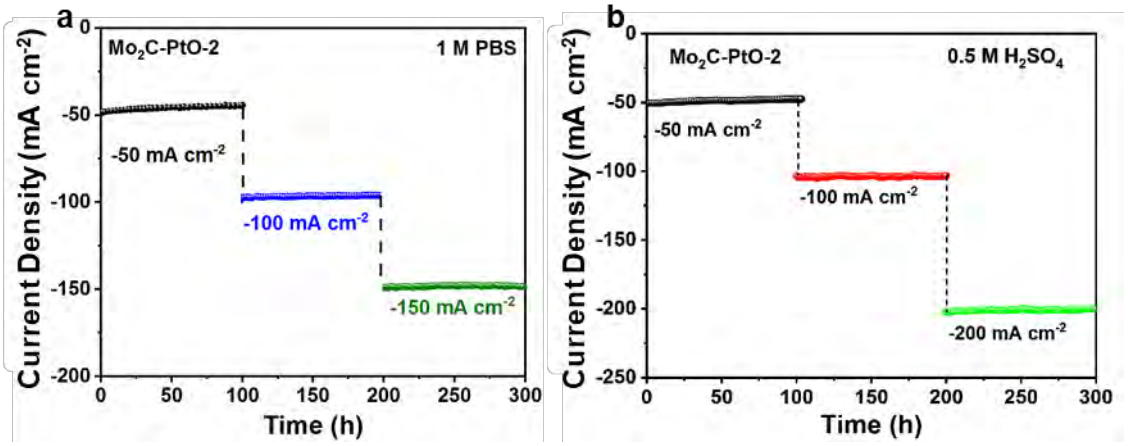

Figure S20 Chronoamperometry test of Mo_2C-PtO-2 at different initial current density in 1 M PBS and 0.5 M H_2SO_4 for 300 h, respectively.

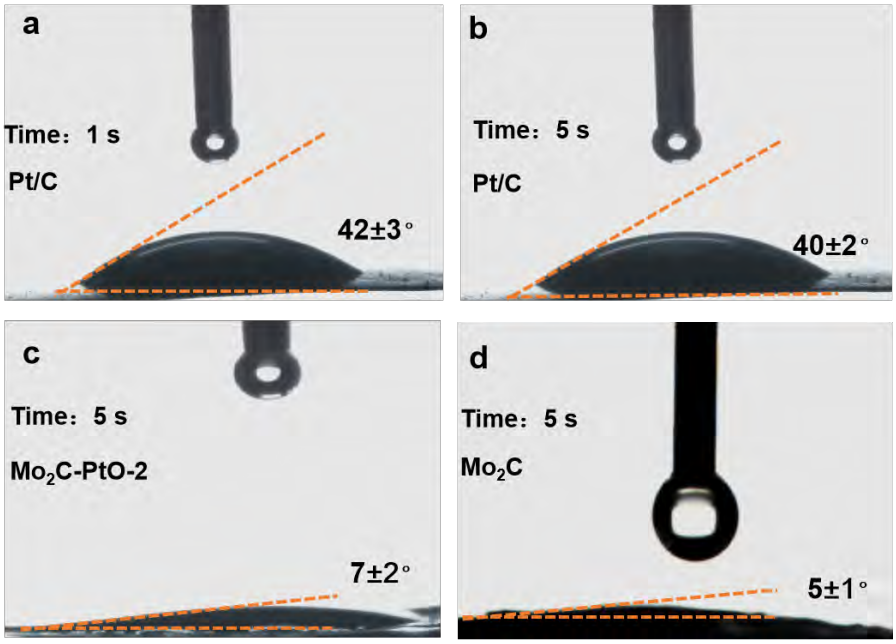

Figure S21 Water contact angle measurement of commercial Pt/C, Mo_2C-PtO-2 and 2D Mo_2C samples.

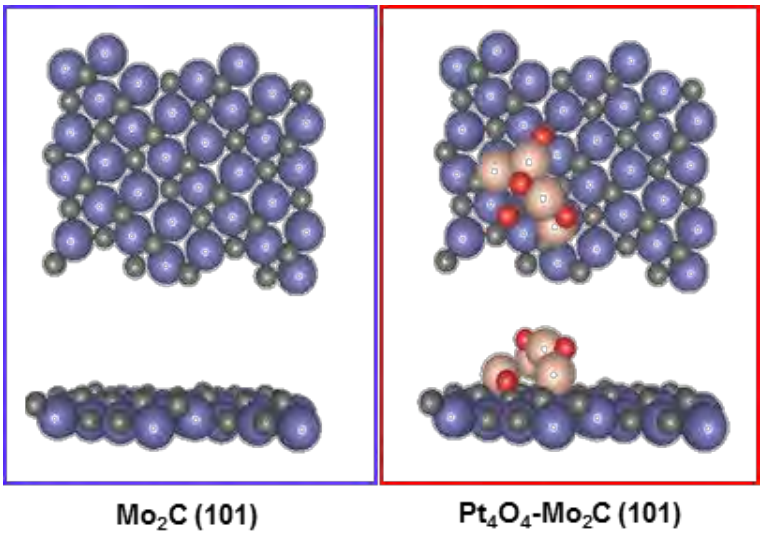

Figure S22 The model of Mo_2C (101) and Pt_4O_4 cluster decorated Mo_2C (101).

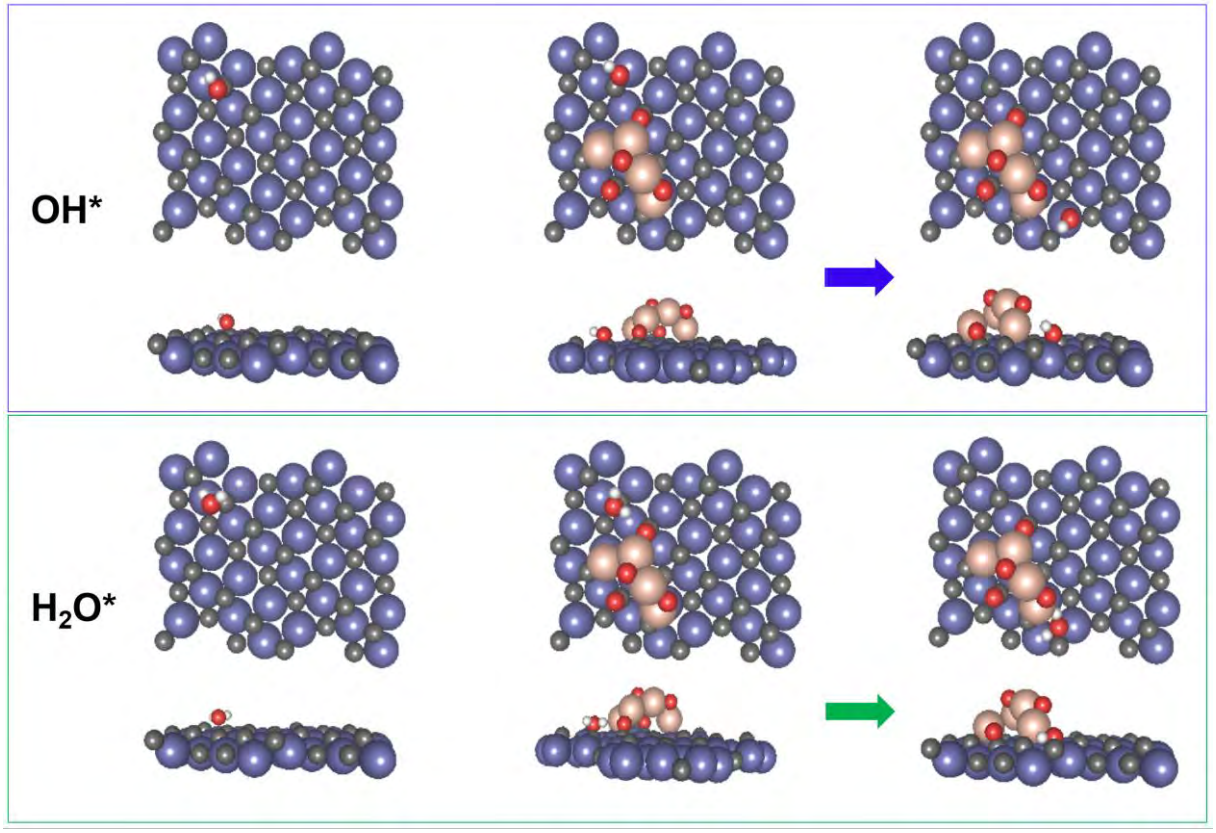

Figure S23 Schematic illustration of adsorption of OH*, and H_2O* on Mo_2C (101) and Pt_4O_4-Mo_2C (101).

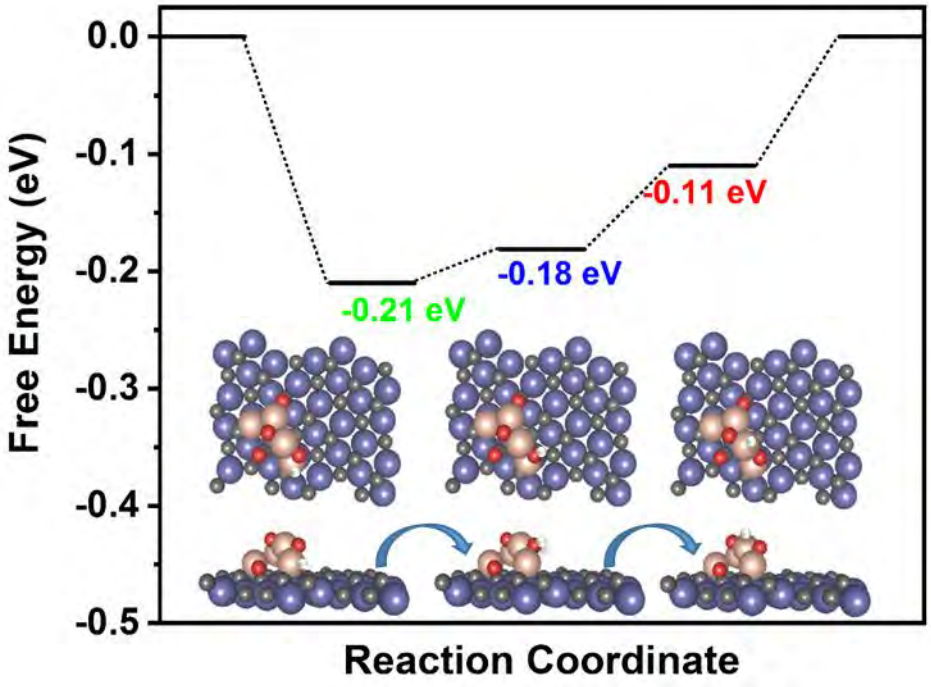

Figure S24 Schematic illustration of adsorption free energy of H atom at top, side Pt sites and the bridged O site.

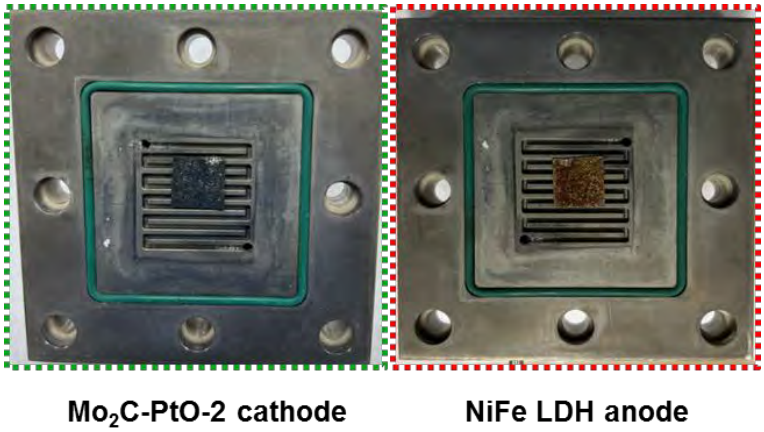

Figure S25 Digital photograph of AEM-WE device assembled with Mo_2C-PtO-2 cathode and NiFe LDH anode.

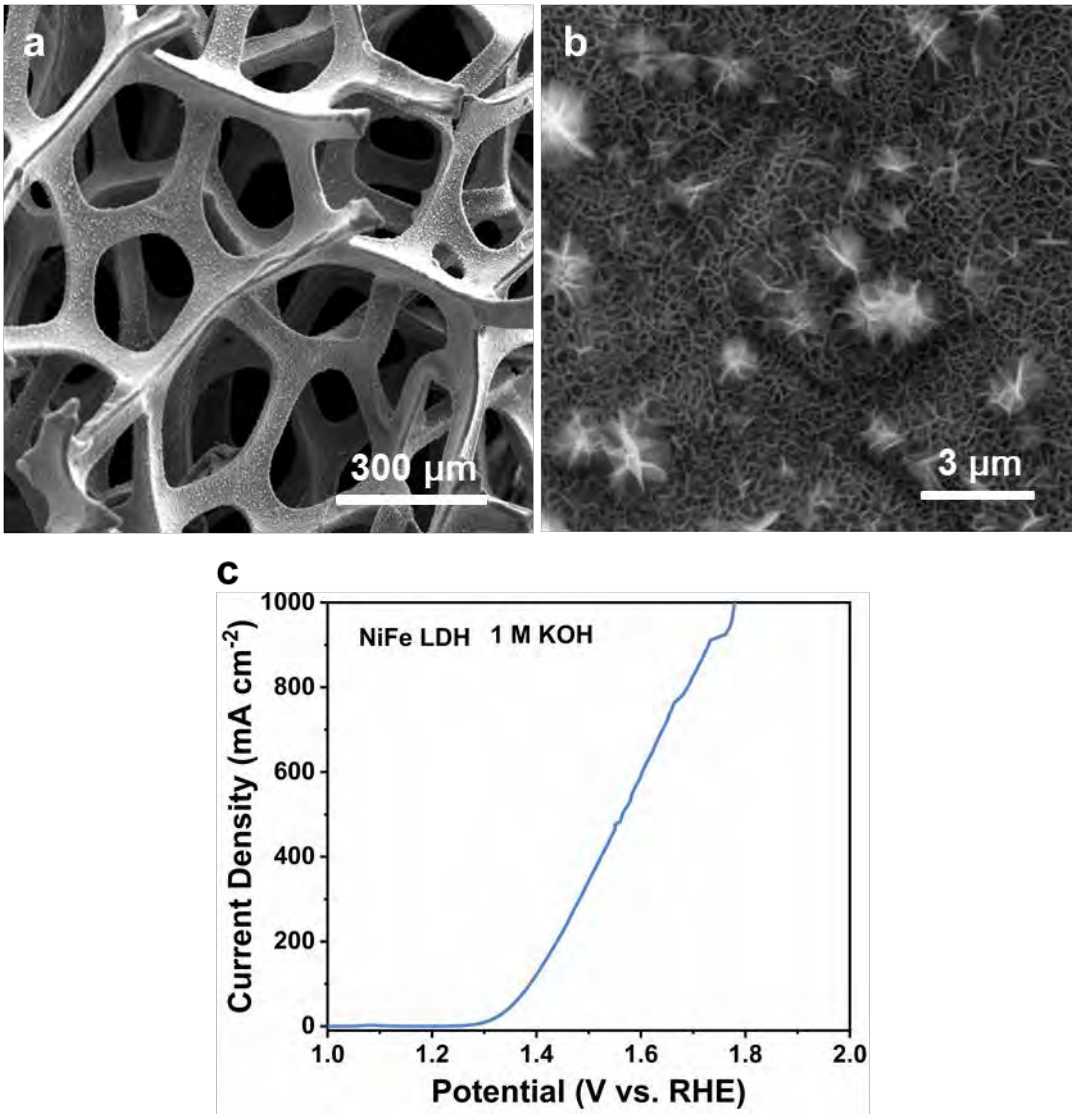

Figure S26 (a), (b) SEM image of NiFe LDH on Ni foam; (c) Corresponding LSV curves in 1 M KOH.

Table S1 Comparison of the HER activity of the Mo_2C-PtO catalyst with that of most relevant platinum-based catalysts under alkaline conditions.

Catalysts	**Overptential (mV) (At 10 mA cm^{-2})**	**References**
Mo_2C-PtO-2	**5**	**This work**
MoN-5%Pt	11.2	Adv. Funct. Mater., 33 (2023) 2302297
Pt/MoP@NC	23.4	Inorg. Chem., 62 (2023) 8719–8728
NiPt-Mo_2C	25.2	Green Energy Environ., 8 (2023) 559–566
Pt/NiO-300	28	Nano Lett., 21 (2023) 4845
Ni_2P/CoP-Pt	44.5	Adv. Funct. Mater., 33 (2023) 2209967
$Ni(OH)_2$-PtO_2	60	J. Mater. Chem. A, 6 (2023) 1967-1970